

C-Tubes: Design and Optimization of Tubular Structures Composed of Developable Strips

MICHELE VIDULIS*, EPFL, Switzerland

KLARA MUNDILOVA*, EPFL, Switzerland

QUENTIN BECKER*, EPFL, Switzerland

FLORIN ISVORANU, EPFL, Switzerland

MARK PAULY, EPFL, Switzerland



Fig. 1. A trefoil lamp assembled from developable surface strips. This C-tube has been optimized to perfectly align the triangular profiles at the start and end point of the input trefoil curve in a way that results in a single developable surface strip for the whole model. This strip is cut into segments for fabrication as shown on the left. The photos show the physical model with an interior light from different viewpoints.

We introduce *C-tubes*, 3D tubular structures composed of developable surface strips. C-tubes can be understood as a generalization of Monge surfaces—a special class of sweep surfaces—towards the recently introduced conesets. This observation allows formulating a constructive algorithm to create tubular structures that ensures developability of the constituent surfaces, while significantly broadening the design space. Our novel form-finding tool enables design exploration by solving for the input variables of the constructive algorithm so that the C-tube best conforms to user-specified objectives. We discuss several case studies that illustrate the versatility of our approach for the design and fabrication of complex structures, with applications in architecture, furniture, and lighting design.

CCS Concepts: • Applied computing → Computer-aided design.

ACM Reference Format:

Michele Vidulis, Klara Mundilova, Quentin Becker, Florin Isvoranu, and Mark Pauly. 2025. C-Tubes: Design and Optimization of Tubular Structures Composed of Developable Strips. *ACM Trans. Graph.* 44, 4 (August 2025), 19 pages. <https://doi.org/10.1145/3730933>

*joint first authors.

Authors' addresses: Michele Vidulis, michele.vidulis@epfl.ch, EPFL, Switzerland; Klara Mundilova, klara.mundilova@epfl.ch, EPFL, Switzerland; Quentin Becker, quentin.becker@epfl.ch, EPFL, Switzerland; Florin Isvoranu, florin.isvoranu@epfl.ch, EPFL, Switzerland; Mark Pauly, mark.pauly@epfl.ch, EPFL, Switzerland.

Permission to make digital or hard copies of all or part of this work for personal or classroom use is granted without fee provided that copies are not made or distributed for profit or commercial advantage and that copies bear this notice and the full citation on the first page. Copyrights for components of this work owned by others than the author(s) must be honored. Abstracting with credit is permitted. To copy otherwise, or republish, to post on servers or to redistribute to lists, requires prior specific permission and/or a fee. Request permissions from permissions@acm.org.

© 2025 Copyright held by the owner/author(s). Publication rights licensed to ACM. 0730-0301/2025/8-ART \$15.00 <https://doi.org/10.1145/3730933>

1 INTRODUCTION

Complex freeform geometries find application in numerous domains, e.g., in the design of architectural structures, engineering components, consumer products, or medical parts. Mapping a digital model to cost- and material-efficient fabrication processes is critical in these domains, which has motivated research efforts on fabrication-aware computational design [Bermano et al. 2017].

Shaping complex curved shapes from planar, but flexible or foldable sheet material is one prominent example of a specialized manufacturing process that can lead to significant cost savings. This approach is relevant across a wide range of applications and scales, from architectural freeform facades, to origami-inspired deployable space structures, furniture design, kirigami-based materials, down to the design of micro-scale foldable robots [Yuan et al. 2023].

Mathematically, we can model surfaces that can be unrolled into the plane without stretching or tearing as *developable surfaces*. These surfaces are characterized by the existence of a family of ruling lines along which the tangent planes remain constant [Pottmann and Wallner 2010]. Equivalently, developable surfaces can be understood as surfaces with zero intrinsic curvature, implying local isometry to a plane. This property, despite being particularly attractive for fabrication, translates into severe constraints for a globally smooth surface to be developable, and extensive work has been done on the design of piecewise developable surfaces. Such surfaces can be decomposed into single-curved developable patches that admit tangent discontinuities along the connecting boundaries, allowing for more design flexibility.

In this paper, we explore tubular structures composed of developable strips, that is, elongated patches of developable surfaces (see

Figure 1). Geometrically, such structures can be modeled as sweep surfaces, where a profile curve is swept along a 3D space curve. We model the profile curve as a (possibly non-planar) polygon and focus on cases where the resulting sweep surface is composed of developable surface strips. We call such structures *C-tubes* to emphasize their connection to *cone-nets*, which will be discussed below.

While reducing cost and simplifying assembly, the developability constraint is challenging to enforce *a posteriori* through optimization, often resulting in significant deviations from the initial design. We therefore propose a computational design and form-finding method that guarantees exact developability by construction. To achieve this goal, we make the following technical contributions:

- We present a theoretical analysis that provides a classification of the design space of C-tubes and establishes relations to existing surface constructions for discrete and continuous developable surfaces.
- Building upon insights of our analysis, we propose a constructive technique to create C-tubes that is simple to implement and guarantees developability by construction.
- We introduce a numerical optimization method for C-tubes that solves for the input variables of the constructive algorithm to best match the resulting C-tube to user-specified design objectives.

We present a series of design studies that illustrate the versatility of our approach for the design of complex 3D structures with applications across a range of scales. Prototypes constructed from different sheet materials validate our computational design method. All geometric models, the complete source code, and all algorithm parameters are available at <https://go.epfl.ch/c-tubes>.

Overview. The remainder of the paper is organized as follows. We first summarize related work in Section 2, before discussing cone-nets and Monge surfaces in more detail. These two surface classes are relevant since our method can be seen as an implementation of (semi-) discrete cone-nets that generalize Monge surfaces. Specifically, in Section 3 we introduce a generalization of Monge surfaces that inherits the simplicity of their constructive approach while providing a significantly expanded design space to better meet user constraints. This additional flexibility is exploited in a form-finding optimization presented in Section 4 that solves for the centerline curve and all other relevant shape parameters of a C-tube, while ensuring developability of its surface strips by construction. In Section 5, we illustrate how our method can be used for challenging design tasks, discuss its limitations, and propose areas for future research. We provide a more in-depth study of the properties of C-tubes in the Appendix. In particular, we show how to design torsion-free support structures for C-tubes and discuss how our approach can be used to construct special classes of cone-nets.

2 BACKGROUND AND RELATED WORK

Joining or gluing developable patches along their curved boundaries can produce a wide variety of free-form geometries with diverse topologies, including open discs, tubes, spheres, or even higher-genus structures. In this section, we examine related work on shapes derived from developable patches and provide an overview of the background on cone-nets and Monge surfaces.



Fig. 2. A design study of a lighting fixture cast from transparent acrylic. Parts of the C-tube mold used for casting are indicated on the left.

2.1 Shapes from Developable Patches

Research on structures composed of developable patches focused on several questions, including:

- (1) Given a target shape, how can it be approximated using developable patches?
- (2) Conversely, given a predefined set of developable patches and an understanding of how to connect them along their boundaries, how can the resulting shape be determined?
- (3) Given a target shape and a constructive design concept, how can this concept be effectively applied to derive functional shapes composed of developable patches?

The tools used to explore these questions are diverse, encompassing experimental fabrication, differential geometric analysis, and advanced computational methods for modeling, optimization, and simulation.

This paper mainly contributes to the third research question by presenting a theoretical framework and computational approach for approximating a given curve (or network of curves) with tubular structures composed of developable strips. For completeness and to highlight the general complexity and interdisciplinary interest in computational design with developable patches, we also discuss related work addressing the other questions. It is important to note that some works discussed below contribute to approaches addressing multiple of the above research questions.

Approximation of Shapes Using Developable Patches. The use of strip models provides valuable educational and visual insights into representing specific surface classes. For example, [Sauer 1942] employs discretizations and strip models to illustrate concepts from smooth differential geometry.

Analytical approximation of shapes with developable patches and their topological implications have also been the subject of recent studies. Inspired by rolling shapes, Raffaelli et al. [2016; 2018] find analytical approximations of surfaces using Cartan ribbons. The special case of surface foliations along geodesic curves has been studied by Branden and Gravesen [2017; 2018]. This case is closely related to the Monge surfaces discussed in Section 2.3.

Computationally, the approximation by developable patches is addressed by [Stein et al. 2018] using a variational approach on triangular meshes, by [Sellán et al. 2020], who enforce developability on height fields, and by [Ion et al. 2020], who use discrete orthogonal

nets. The remeshing of triangle meshes representing piecewise developable surfaces to planar quad dominant meshes is considered in [Verhoeven et al. 2022]. Approximating sketched boundaries with developable patches is explored by [Rose et al. 2007]. Motivated by architectural applications, the generation of strip models using refinement and optimization is discussed by [Liu et al. 2006].

A special case occurs when developable patches are joined to form a disc-like geometry that is globally developable, that is, the individual developable patches can be placed next to each other with no gaps between them. This property allows the resulting shape to be fabricated through folding along curves, a process often referred to as *curved crease origami*. [Kilian et al. 2008] develop a framework for design and approximation of developables with curved creases, using a planar quad dominant mesh. Encoding patches as $2 \times n$ B-spline surfaces and optimizing their control points for developability is subject of explorations in [Pottmann et al. 2008; Tang et al. 2016].

Generation of Shapes by Joining Developable Patches. Rather than cladding given surfaces with developable patches, the exploration of shapes formed by joining developable patches has also been a topic of investigation. A prominent example are D-forms, created by joining two developable patches with equal perimeter along their boundaries to form closed volumes. First introduced by [Wills 2006], D-forms were formalized by [Pottmann and Wallner 2010] and further analyzed by [Demaine and Price 2010].

While D-forms can be readily fabricated manually, their analytical description is complex, and only a few parametrizations are known. For example, the parametrization of the *squircle*, a D-form created by gluing the boundaries of a square and a circle, is discussed by [Mundilova 2024, Chapter 9]. Using their publicly available modeler TopMod3D [Akleman et al. 2008], Xing et al. [2012] design D-forms with tubular handles. Recent work by [Huang et al. 2023] provides an optimization-based framework for the exploration of D-forms.

David Huffman was one of the first to systematically study the behavior of paper when folded along curved creases, see [Demaine et al. 2011; Koschitz 2014]. Today, David Huffman’s designs continue to serve as a foundation for theoretical exploration [Demaine et al. 2018]. Computationally, the design and reconstruction of complex curved crease shapes using optimization have been explored through planar quad-dominant meshes [Solomon et al. 2012] and discrete orthogonal geodesic meshes [Rabinovich et al. 2019].

Application of Design Concepts to Target Shapes. Designing with developable patches for functional purposes is inherently challenging and often demands customized solutions. In addition to the work discussed above, several approaches have focused on applying selected design paradigms to target shapes.

Inspired by tessellations of David Huffman discussed in [Demaine et al. 2015], approximating polyhedral shapes (target) using curved crease modules in the shape of lenses (design concept) was explored by [Stern and Maleczek 2018] and [Kraft et al. 2023]. In the latter work, as in our approach, local developability is inherently ensured by construction, while optimization techniques are employed to achieve global developability.

Another notable example is the work by [Jiang et al. 2019] on the computational treatment of curve-pleated structures. In their work, the target shapes are curves or surfaces that are approximated using

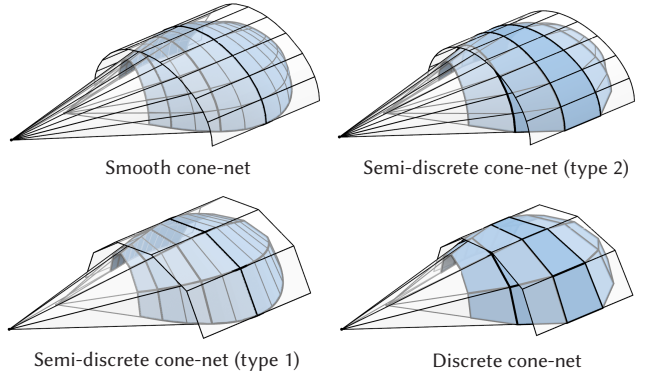


Fig. 3. Illustration of cone-nets and their smooth or discrete tangential cylinders and cones. We focus on the cone-nets shown in the bottom row.

discretized curved pleats as the design concept. The authors enforce the two constraints, curved crease and developability, through optimization applied to the vertices of discretized meshes. In contrast, our method only considers local developability, which is inherently satisfied through the construction process.

Focusing on foldability, [Tachi 2013] introduced composite curved crease origami structures composed of rigidly foldable tubes along curves. Structures that approximate networks of curves with curved creases were studied in [Chandra et al. 2015], while multilayered foldable shells were explored in [Bernhard and Maleczek 2023]. In this paper, we explore the generation and optimization of tubular structures composed of developable strips and their discrete counterparts, focusing on individual patches and their local rather than global developability, which offers more flexibility for design.

The recent method of [Maekawa and Scholz 2024] can be used to build tubular structures with developable strips using rotation-minimizing frames. This choice limits the results to Monge surfaces. We show a comparison to this approach in Section 5.

2.2 Cone-nets

In recent work by [Kilian et al. 2023], the authors investigate *smooth cone-nets*, that is, surface parametrizations where the enveloping developables of one family of parameter curves are cylinders or cones, rather than generic developable surfaces.

Locally, any surface can be reparametrized as a cone-net. For an intuitive explanation of the corresponding geometric construction, see Section 2.1 of [Kilian et al. 2023], which generalizes an approach originally described by [Böken 1884]. In addition to studying the properties of such parametrizations, Kilian and coauthors also discuss their discrete counterparts, discrete cone-nets, which are regular planar quad (PQ) meshes with one family of strips lying on discrete cones or cylinders. Discrete cone-nets should not be confused with conical nets, which are PQ meshes where the adjacent faces around each vertex are in tangential contact with a cone of revolution [Liu et al. 2006].

Prominent examples of cone-nets are *T-surfaces*, characterized by smooth or discrete parameter lines that lie in two orthogonal families of planes [Izmestiev et al. 2024], resulting in surfaces where

one parameter family is tangent to cylinders. The discrete analogues of T-surfaces, known as *T-hedra*, consist of trapezoidal faces. Originally described by [Graf and Sauer 1931] as a class of flexible quad-surfaces, T-surfaces and T-hedra, particularly in tubular shape, remain an active area of research in computational origami, see [Sharifmoghaddam et al. 2023, 2020]. Another example of rigidly foldable discrete cone-nets are horn-shaped mechanisms composed of Bricard octahedra [Tachi 2016].

Although not discussed in detail by [Kilian et al. 2023], there are two semi-discrete types of cone-nets, obtained by refining either parameter direction of a discrete cone-net (see Figure 3). The first type, which we refer to as *type 1*, is obtained by refining the non-conical strips and consists of general strips of developable surfaces (see inset figure on the right), where the tangent planes along consecutive rulings are tangent to a cone. The second type, obtained by refining conical PQ strips, combines conical strips.

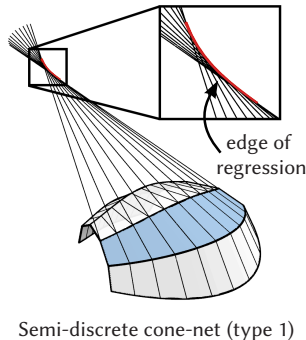
In the following, we focus on tubular structures that are semi-discrete cone-nets of the first type, characterized by ruling polylines forming closed loops, as well as their discrete counterparts.

2.3 Monge Surfaces

A relevant subclass of cone-nets are Monge surfaces, widely used in computer-aided design. They are constructed using two curves: a space curve, known as the *directrix*, and a planar curve, the *generatrix*. The generatrix is swept along the directrix in a rotation-minimizing manner. Both curves can either be smooth or discrete.

2.3.1 Smooth Directrix. If the directrix is smooth, the surface's parametrization can be described using a rotation minimizing frame of the directrix, see [Klok 1986]. The resulting parametrization of Monge surfaces is a principal line parametrization, and the congruent planar parameter lines parallel to the generatrix are geodesics on the surface. Additionally, if the generatrix is discrete, the developable strips composing the sweep surface have rulings perpendicular to the tangents of the directrix-parallel curves. The envelopes of tangent planes along generatrix-parallel curves form cylinders.

2.3.2 Discrete Directrix. If the directrix is a polyline, the surface can be described constructively by starting with an appropriately positioned generatrix. The last generatrix-parallel curve is extruded along the edges of the directrix, intersected with the plane that bisects the angle between adjacent edges, and the resulting intersection forms the next generatrix-parallel curve. It is important to note that computing the intersection with the bisecting plane is a locally “rotation minimizing” operation. The transformation that converts a vector perpendicular to one edge into a vector perpendicular to another edge with minimal rotation is a reflection across the bisecting planes of the edges [Gonzalez-Quintial and Martín-Pastor 2024].



Semi-discrete cone-net (type 1)

Depending on whether the generatrix is smooth or discrete, the resulting surface is semi-discrete or discrete, respectively, and consists of smooth or discrete cylinders with congruent profile curves and rulings parallel to the edges of the directrix.

2.3.3 Properties. Discrete Monge surfaces consist of conical vertices, as the sums of the opposite angles at each vertex are the same. Consequently, they enable mesh-offset support structures, making them popular in the architectural design of freeform facades [Mesnil et al. 2015]. The conical vertices of Monge surfaces also find application in foldable structures, as discussed in the theory of flexible structures, particularly as rigidly-foldable tubes [Filipov et al. 2016].

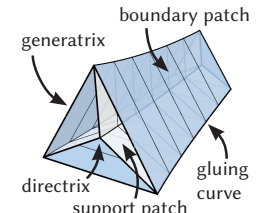
While Monge surfaces are straightforward to implement and manipulate, their design space is limited. In particular, the construction yields families of surfaces where one family of parameter lines is always coplanar, while the other family features parallel tangents.

3 C-TUBES

Inspired by the Monge surface construction, we introduce an intuitive design framework for tubular structures composed of developable surfaces that correspond to semi-discrete cone-nets with a closed discrete generatrix. We refer to them as *C-tubes with a smooth directrix*, or simply *smooth C-tubes*. We also highlight their discrete counterparts, which are *C-tubes with a discrete directrix* or *discrete C-tubes*. Analogously, we refer to Monge surfaces with a closed discrete generatrix as *smooth* and *discrete M-tubes*.

We use both the terms *patches* and *strips* to describe bounded regions of smooth and discrete surfaces. The directions of the edges of a discrete curve will be referred to as its tangents, where the tangent at a vertex is defined as the direction of the outgoing edge.

We use the term *gluing curves* to describe the curves connecting two boundary patches. The ruled patches between the directrix and the gluing curves, which we assume are formed by connecting points on the directrix and gluing curves corresponding to the same parameter value, are referred to as *support patches* (see also Figure 4).



3.1 Main Idea

Our design framework for C-tubes is inspired by a two-fold generalization of Monge surfaces. This approach is based on the following observations (see Figure 4, left):

OBSERVATION 1. *In both smooth and discrete M-tubes, the support patches are developable. For smooth M-tubes, the rulings of the support patches lie in planes perpendicular to the tangent of the directrix. For discrete M-tubes, the rulings of the support patches lie in planes bisecting consecutive edges of the directrix and gluing curves.*

OBSERVATION 2. *In both smooth and discrete M-tubes, the tangents of the directrix and gluing curves are parallel. For smooth M-tubes, the tangents of the directrix and gluing curves are perpendicular to the rulings of the support patch. For discrete M-tubes, the edges of the directrix and gluing curves enclose the same angle with the incident rulings of the support patch.*

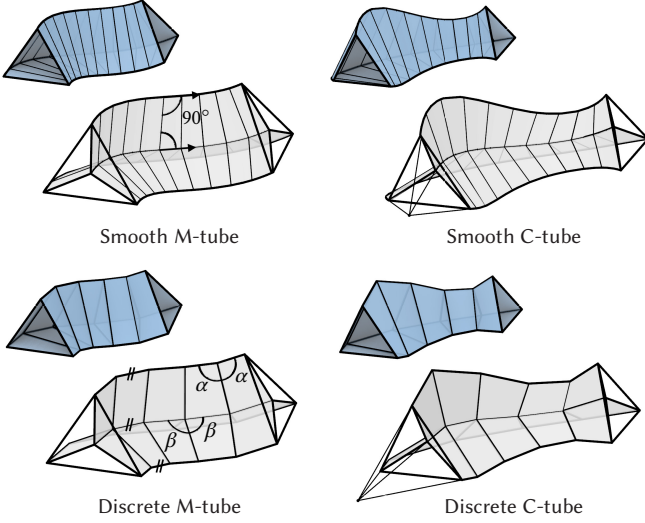


Fig. 4. M-tubes (left) are a special case of C-tubes (right). The developable boundary strips are shown in blue, the support strips connecting the directrix with the gluing curves are shown in grey.

Inspired by the above observations, we generalize the construction of Monge surfaces from a given directrix in two ways:

GENERALIZATION 1. *Instead of restricting support patches to those with rulings perpendicular to the tangents of the directrix, we allow the support patches to be general smooth or discrete developables.*

GENERALIZATION 2. *Rather than only permitting the gluing curves to be parallel to the directrix, we consider gluing curves whose tangent lines converge to a point on the corresponding tangent line of the directrix, forming a discrete cone.*

The condition in the second generalization ensures the smooth and discrete developability of the boundary patches, as it guarantees that neighboring corresponding tangents are coplanar. In the smooth case, these coplanar tangents span the incident tangent plane. In the discrete case, this plane contains the face of the boundary patches. In Appendix D we discuss the construction of a special class of cone-nets using our approach.

3.2 Construction Overview

To highlight the similarities between smooth and discrete C-tubes, we unify their notations in the exposition that follows. The primary distinction lies in the directrix, which is parametrized over a continuous interval $T = [t_0, t_{\max}]$ in the semi-discrete case, and over a discrete set of M values $T = \{t_0, \dots, t_{M-1}\}$ in the discrete case.

The inputs of our C-tube construction algorithm are:

- A directrix $X(t) : T \rightarrow \mathbb{R}^3$.
- A discrete generatrix $G_{0,0}, \dots, G_{N-1,0}$, consisting of N vertices. If the generatrix is closed, then $G_{0,0} = G_{N-1,0}$.
- N families of *construction planes* $\Pi_0(t), \dots, \Pi_{N-1}(t)$, one for each vertex of the generatrix along the tube. Each plane $\Pi_i(t)$ is incident to the corresponding point along the directrix, $X(t) \in \Pi_i(t)$, and has unit normal vectors $P_i(t) : T \rightarrow S^2$. To

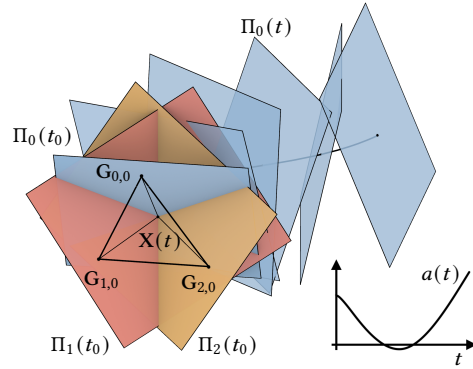


Fig. 5. Illustration of the inputs to the C-tube construction algorithm discussed in Section 3.2 used to generate the smooth C-tube in Figure 4.

avoid degeneracy, we require $\Pi_i(t)$ to exclude the incident tangent of the directrix, that is, $P_i(t) \cdot X'(t) \neq 0$ in the smooth case, and both $P_i(t_j) \cdot (X(t_j) - X(t_{j-1})) \neq 0$ and $P_i(t_j) \cdot (X(t_{j+1}) - X(t_j)) \neq 0$ in the discrete case. Additionally, we require that the vertices of the provided generatrix belong to the corresponding planes at $t = t_0$, that is, $G_{i,0} \in \Pi_i(t_0)$.

- A scalar-valued *apex-locating function* $a(t) : T \rightarrow \mathbb{R}$, which determines the location of the cone apices on the tangents of the directrix.

These parameters, illustrated in Figure 5, span the full design space of C-tubes as we discuss below. For computations in the smooth case, we assume that $X(t) \in C^2$, $P_i(t) \in C^1$, and $a(t) \in C^1$.

In a typical design tasks, the directrix and generatrix are provided by the user, in addition to various constraints, such as tangency alignment requirements (see also Section 5). The construction planes and apex-locating function are in general not intuitive parameters to set and tune in a design process. The algorithm presented in Section 4 optimizes for these parameters and allows the designer to explore the shape space of C-tubes by specifying more intuitive constraints and objectives.

3.3 C-Tube Construction

Constructing a C-tube from the above input amounts to computing N gluing curves $G_i(t)$, with $G_i(t_0) := G_{i,0}$. The $N - 1$ developable patches of the C-tubes are then obtained as

$$D_i(t, u) = (1 - u) G_i(t) + u G_{i+1}(t), \quad \text{where } (t, u) \in T \times [0, 1],$$

with $i \in \{0, \dots, N - 2\}$.

Both the smooth and discrete gluing curves $G_i(t)$, which satisfy the generalizations presented in Section 3.1, can be computed from the following two conditions:

- *Condition 1:* The gluing curves are incident to the construction planes, $G_i(t) \in \Pi_i(t)$, or equivalently,
- $$(G_i(t) - X(t)) \cdot P_i(t) = 0.$$
- *Condition 2:* The tangents of the gluing curves coincide with the apices encoded by the apex-locating function on the tangents of the directrix.

The curves satisfying these constraints are determined up to their initial values and can be computed “sequentially” as the solution of either differential equations or their discrete analogues.

It is important to note that gluing curves satisfying these constraints may result in patches with singularities. While these are not addressed in the following theoretical computation, the optimization framework presented in Section 4 controls the emergence of edges of regression within the width of the boundary patches by introducing dedicated regularization terms.

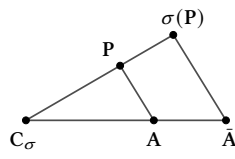
The key insight for the encoding of the second constraint lies in adopting a scale-mapping approach to represent cones and cylinders in a unified manner, enhancing the robustness of computation. This idea is inspired by the approach described by Mundilova, Demaine, and Tachi [2024, Section 12.4] to compute curved creases that connect developable patches with projective cones. Before a detailed discussion of the smooth and discrete constraints, we first review the notation for scale mappings.

3.3.1 Scale Mappings. Given a pair of distinct points \mathbf{A} and $\bar{\mathbf{A}}$ and a scalar value a encoding the scale center, a scale mapping σ that maps \mathbf{A} to $\bar{\mathbf{A}}$ for a generic point \mathbf{P} can be expressed as

$$\sigma : \mathbb{R}^3 \rightarrow \mathbb{R}^3, \quad \mathbf{P} \mapsto a(\mathbf{P} - \mathbf{A}) + \bar{\mathbf{A}}.$$

If $a = 1$, the scale center is at infinity, and the scale mapping reduces to a translation by $\bar{\mathbf{A}} - \mathbf{A}$. Otherwise, as shown on the right, the location of the scale center is given by

$$C_\sigma = \frac{\bar{\mathbf{A}} - a\mathbf{A}}{1 - a}.$$



Note that when $a = 0$, the scale center coincides with $\bar{\mathbf{A}}$, mapping all points directly to $\bar{\mathbf{A}}$. Additionally, unless $\bar{\mathbf{A}} = \mathbf{A}$, there is no real value a that corresponds to \mathbf{A} being the center of scaling C_σ .

In the following construction, the apices of the tangential cones are located on the tangents to the directrix $\mathbf{X}(t)$ and are encoded using scale mappings centered at those cone apices. These scale mappings are determined by the value of the apex-locating function $a(t)$ and by two corresponding points playing the role of \mathbf{A} and $\bar{\mathbf{A}}$ in the definition of σ .

With this approach to encode cone apices, the selection of corresponding points determines which tangential cone apices can be represented with real values. Note that, for numerical reasons, we want to avoid explicitly dealing with the case $a = \infty$. For a discussion of the specific parametrization choice presented in the following section, and its implications in the smooth and discrete case, we refer to Appendix A.

3.3.2 Smooth Directrix. For a smooth directrix, we define a one-parameter family of scale mappings σ_t through the pair of corresponding points $\mathbf{A} = \mathbf{X}(t)$ and $\bar{\mathbf{A}} = \mathbf{X}(t) + \mathbf{T}(t)$ and apex-locating scalar $a(t)$, see Figure 6, left. Then, the second constraint translates to the condition that the vectors $\mathbf{G}'_i(t)$ and $\sigma_t(\mathbf{G}_i(t)) - \mathbf{G}_i(t)$ are parallel. For a detailed exposition why this results in two differential constraints that determine the gluing curve up to appropriate initial values, please refer to Appendix B.

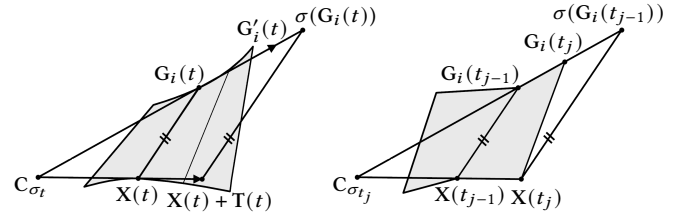


Fig. 6. Illustration of the scale mappings used to compute the gluing curve for smooth (left) and discrete (right) C-tubes.

3.3.3 Discrete Directrix. Similar to the smooth case, the discrete computation of the gluing curve can be formulated as a sequential process for each gluing curve individually. Again, we define a one-parameter family of scale mappings σ_t through corresponding points $\mathbf{A} = \mathbf{X}(t_{j-1})$ and $\bar{\mathbf{A}} = \mathbf{X}(t_j)$ and an apex-locating scalar $a(t_j)$, see Figure 6, right.

Starting from an appropriate initial value $\mathbf{G}_i(t_{j-1})$, we compute the subsequent gluing curve vertex $\mathbf{G}_i(t_j)$ as the intersection of the plane $\Pi_i(t_j)$ with the line connecting $\mathbf{G}_i(t_{j-1})$ and $\sigma_t(\mathbf{G}_i(t_{j-1}))$. Computationally, we parametrize this line as

$$\mathbf{G}_i(t_j) = \mathbf{G}_i(t_{j-1}) + d_{i,j} \mathbf{V}, \quad (1)$$

where

$$\begin{aligned} \mathbf{V} &= \sigma_{t_j}(\mathbf{G}_i(t_{j-1})) - \mathbf{G}_i(t_{j-1}) \\ &= a(t_j)(\mathbf{G}_i(t_{j-1}) - \mathbf{X}(t_{j-1})) + \mathbf{X}(t_j) - \mathbf{G}_i(t_{j-1}), \end{aligned} \quad (2)$$

and compute the initially unknown scalar $d_{i,j}$ from

$$(\mathbf{G}_i(t_j) - \mathbf{X}(t_j)) \cdot \mathbf{P}_i(t_j) = 0.$$

Specifically, if $\mathbf{V} \cdot \mathbf{P}_i(t_j) \neq 0$, that is, the next plane and the line connecting the cone apex with $\mathbf{G}_i(t_{j-1})$ have a real intersection, we obtain

$$d_{i,j} = \frac{(\mathbf{X}(t_j) - \mathbf{G}_i(t_{j-1})) \cdot \mathbf{P}_i(t_j)}{\mathbf{V} \cdot \mathbf{P}_i(t_j)}. \quad (3)$$

Note that the case $\mathbf{V} \cdot \mathbf{P}_i(t_j) = 0$, schematically illustrated in Figure 7, corresponds to pathological configurations that one would want to avoid in practice. In these configurations, either the cone apices are located close (or even belong) to the discrete directrix,

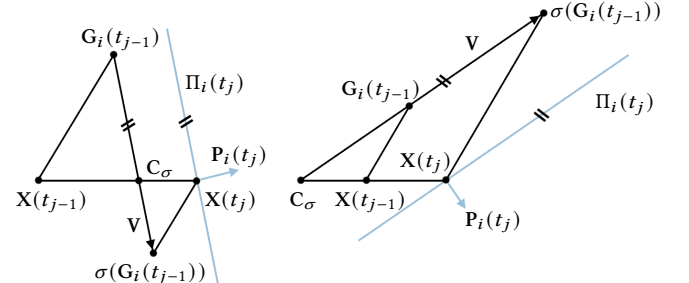


Fig. 7. Two configurations where $\mathbf{V} \cdot \mathbf{P}_i(t_j) = 0$. This can occur either when C_σ is close (belongs) to the directrix (left), or when the plane normal $\mathbf{P}_i(t_j)$ deviates significantly from the directrix tangent (right).

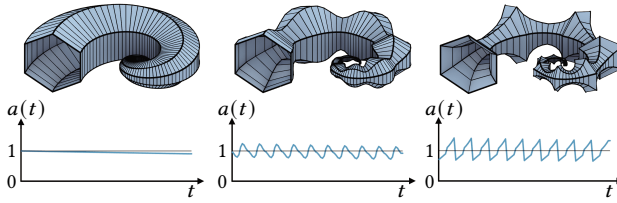


Fig. 8. Three different C-tubes sharing the directrix, the generatrix, and the plane normals, using the apex-locating function displayed at the bottom.

or the plane normals substantially deviate from the directrix tangents. When $a(t_j) = 1$, the condition $\mathbf{V} \cdot \mathbf{P}_i(t_j) \neq 0$ is equivalent to $(\mathbf{X}(t_j) - \mathbf{X}(t_{j-1})) \cdot \mathbf{P}_i(t_j) \neq 0$, introduced in Section 3.2 as an assumption defining admissible plane normals. In our implementation, we regularize the plane normals and the apex-locating function to prevent such cases from occurring, see Section 4.4.

Figure 8 shows three different C-tubes resulting from the same directrix, generatrix, and plane normals, that use three different apex-locating functions.

3.4 Remarks

Setting $a(t) = 1$ for all $t \in T$ ensures that the tangents of the directrix are parallel to the tangents of the gluing curves. To generate smooth or discrete M-tubes, this choice of the apex-locating function is complemented by setting the plane normals as $\mathbf{P}_i(t) = \mathbf{T}(t)$ for all $i \in \{0, \dots, N-1\}$ and $t \in T$ in the smooth case, or as the normals of the bisecting planes of two consecutive edges of the directrix in the discrete case.

This representation, based on using a directrix curve, allows constructing support structures with torsion-free nodes, see Figure 18. More information is provided in Appendix C.

Note that while we show results mostly for closed profile polygons to obtain smooth or discrete C-tubes, the generatrix could also be an open curve. Appendix D highlights how our approach can be used to construct double cone-nets, a class of cone-nets in which both families of PQ strips coincide with discrete cylinders or cones [Kilian et al. 2023].

Algorithm 1 – Discrete C-tube Forward Construction

Input: directrix \mathbf{X} , generatrix $\mathbf{G}_{:,0}$, plane normals \mathbf{P} , apex-locating function \mathbf{a}
Output: gluing curves \mathbf{G}

```

1: for  $j = 1$  to  $M - 1$  do                                ▷ Traverse the directrix
2:   for  $i = 0$  to  $N - 1$  do    ▷ Update the gluing curve vertices
3:      $\mathbf{V} \leftarrow a_j (\mathbf{G}_{i,j-1} - \mathbf{X}_{j-1}) + \mathbf{X}_j - \mathbf{G}_{i,j-1}$       ▷ (2)
4:     assert  $\mathbf{V} \cdot \mathbf{P}_{i,j} \neq 0$ 
5:      $d_{i,j} \leftarrow \frac{(\mathbf{X}_j - \mathbf{G}_{i,j-1}) \cdot \mathbf{P}_{i,j}}{\mathbf{V} \cdot \mathbf{P}_{i,j}}$           ▷ (3)
6:      $\mathbf{G}_{i,j} \leftarrow \mathbf{G}_{i,j-1} + d_{i,j} \mathbf{V}$            ▷ (1)
7:   end for
8: end for

```

4 C-TUBE OPTIMIZATION

To explore the shape space of C-tubes via optimization, we introduce various objective functions encoding design goals related to local and global geometric properties of a C-tube, such as its cross-sectional shape, thickness, and orientation. We first present our general optimization framework for discrete C-tubes. M-tubes, which are a subset of C-tubes, are used as a didactic example to illustrate the optimization process. We then showcase how the additional degrees of freedom introduced by our generalization of Monge surfaces allow achieving more complex design objectives. Throughout the optimization process, the developability of each boundary patch is always guaranteed exactly thanks to our geometric construction.

4.1 Discrete C-Tubes Construction Algorithm

As discussed in Section 3.3.3, a discrete C-tube can be sequentially computed given a directrix curve, a generatrix, a set of plane normals, and an apex-locating function. The computation is summarized in Algorithm 1.

For brevity, in the following we denote $\mathbf{X}_j = \mathbf{X}(t_j)$, $\mathbf{G}_{i,j} = \mathbf{G}_i(t_j)$, $\mathbf{P}_{i,j} = \mathbf{P}_i(t_j)$, and $a_j = a(t_j)$, with colons replacing an index to indicate the corresponding one-parameter family. Using this convention, we can equivalently express the generatrix as $\mathbf{G}_{:,0}$. Bold letters without indices refer to the full set of values of the corresponding quantity. For example, \mathbf{X} indicates the points of the discrete directrix.

The forward construction produces as output the N discrete gluing curves $\mathbf{G}_{i,:} = \{\mathbf{G}_{i,0}, \dots, \mathbf{G}_{i,M-1}\}$ for $i \in \{0, \dots, N-1\}$, which we gather in $\mathbf{G} = \mathbf{G}(\mathbf{X}, \mathbf{G}_{:,0}, \mathbf{P}, \mathbf{a})$. Thanks to the simplicity of our geometric encoding, the implementation of the forward construction takes as few as 30 lines of Python code, making use of only standard linear algebra and geometry routines for vector and matrix operations. This constructive algorithm is the core component of our optimization framework.

4.2 Optimization Overview

We formulate a set of design objectives as a scalar-valued function of the tube parameters $(\mathbf{X}, \mathbf{G}, \mathbf{P}, \mathbf{a}) \mapsto J(\mathbf{X}, \mathbf{G}, \mathbf{P}, \mathbf{a})$, which we aim to minimize. We assume $\tilde{\mathbf{X}}(t)$ is a user-provided curve representing the directrix of a desired C-tube, which can be specified in any format, e.g. as a polyline, a smooth parametric curve, or a spline

Algorithm 2 – General Optimization of a C-tube

Input: initial tube parameters $(\mathbf{Q}, \mathbf{P}, \mathbf{a}, \theta)$, generatrix $\mathbf{G}_{:,0}$, number of vertices along the directrix M , objective function J
Output: optimal tube parameters $(\mathbf{Q}^*, \mathbf{P}^*, \mathbf{a}^*, \theta^*)$

```

1: do
2:    $\mathbf{X} \leftarrow \text{Sample}(\mathbf{Q}, M)$ 
3:    $\mathbf{G}_{:,0} \leftarrow \text{Rotate}(\mathbf{G}_{:,0}, \mathbf{X}_1 - \mathbf{X}_0, \theta)$     ▷ Rotate about tangent
4:    $\mathbf{G} \leftarrow \text{Construct}(\mathbf{X}, \mathbf{G}_{:,0}, \mathbf{P}, \mathbf{a})$            ▷ Algorithm 1
5:    $\partial \tilde{J} \leftarrow \partial \mathbf{Q} \tilde{J}, \partial \mathbf{P} \tilde{J}, \partial \mathbf{a} \tilde{J}, \partial \theta \tilde{J}$     ▷ Eval. grad. at  $(\mathbf{X}, \mathbf{G}, \mathbf{P}, \mathbf{a})$ 
6:    $\mathbf{d}_Q, \mathbf{d}_P, \mathbf{d}_a, \mathbf{d}_\theta \leftarrow \text{L-BFGS}(\mathbf{Q}, \mathbf{P}, \mathbf{a}, \theta, \partial \tilde{J})$     ▷ Descent dir.
7:    $\mathbf{Q}, \mathbf{P}, \mathbf{a}, \theta \leftarrow \text{Linesearch}(\mathbf{Q}, \mathbf{P}, \mathbf{a}, \theta, \mathbf{d}_Q, \mathbf{d}_P, \mathbf{d}_a, \mathbf{d}_\theta, \tilde{J})$ 
8: while not Converged( $J(\mathbf{X}, \mathbf{G}, \mathbf{P}, \mathbf{a})$ )

```

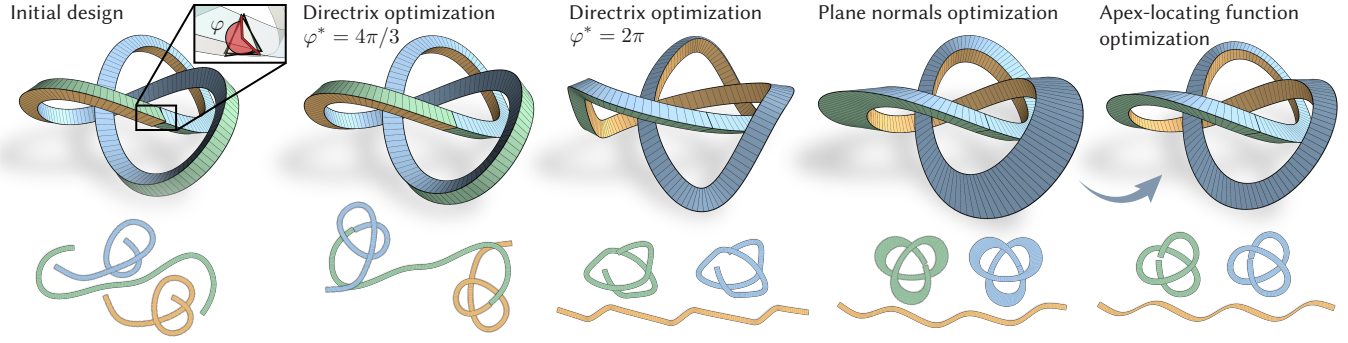


Fig. 9. Optimization of a knotted C-tube for continuous closure. In the initial design generated with a rotation-minimizing frame, the surface strips do not align at their ends. Smoothly closed C-tubes can be obtained by optimizing the directrix, with different results depending on the defect angle φ . An angle of $4\pi/3$ creates a single continuous strip that wraps around the knot three times, while an integer multiple of 2π results in three separate strips. Alternatively, we can achieve smooth closure by optimizing over the plane orientations, which can be combined with scale optimization to retain a more even strip width.

curve. To parametrize the set of smooth curves approximating $\widehat{\mathbf{X}}(t)$, we fit an interpolating cubic spline by sampling $\widehat{\mathbf{X}}(t)$ at K locations $\mathbf{Q}_k = \widehat{\mathbf{X}}(\hat{t}_k)$, where \hat{t}_k are equispaced parameter values. We gather the resulting points in $\mathbf{Q} = \{\mathbf{Q}_0, \dots, \mathbf{Q}_{K-1}\}$, and call the interpolating spline $\mathbf{X}_Q(t) : [0, 1] \rightarrow \mathbb{R}^3$. We then sample \mathbf{X}_Q at M equispaced parameter values to obtain the discrete directrix as $\mathbf{X} = \{\mathbf{X}_0, \dots, \mathbf{X}_{M-1}\}$, with $\mathbf{X}_j = \mathbf{X}_Q(t_j)$ and $t_j = j/(M-1)$.

We represent the plane normals as unit vectors $\mathbf{P}_{i,j} \in S^2$ associated to vertices of the gluing curves and collectively refer to them as \mathbf{P} . When a single plane normal is chosen at each directrix point, i.e., when $\mathbf{P}_{i_1,j} = \mathbf{P}_{i_2,j}$ for all $i_1, i_2 \in \{0, \dots, N-1\}$, $j \in \{0, \dots, M-1\}$, the set reduces to $\mathbf{P} = \{\mathbf{P}_0, \dots, \mathbf{P}_{M-1}\}$. The apex-locating function is discretized as $\mathbf{a} = \{a_0, \dots, a_{M-1}\}$, with $a_j \in \mathbb{R}$. To additionally allow rotations of the initial generatrix about the incident tangent of the directrix, we parametrize the corresponding degree of freedom using the angle θ .

Our general optimization problem minimizes the objective function with respect to the points \mathbf{Q} , the plane normals \mathbf{P} , the apex-locating values \mathbf{a} , and the initial rotation of the generatrix θ as

$$\underset{\mathbf{Q}, \mathbf{P}, \mathbf{a}, \theta}{\operatorname{argmin}} \tilde{J}(\mathbf{Q}, \mathbf{P}, \mathbf{a}, \theta), \quad (4)$$

with

$$\tilde{J}(\mathbf{Q}, \mathbf{P}, \mathbf{a}, \theta) := J(\mathbf{X}(\mathbf{Q}), \mathbf{G}, \mathbf{P}, \mathbf{a}),$$

where \mathbf{G} in turn depends on \mathbf{Q} via \mathbf{X} , on \mathbf{P} , on \mathbf{a} , and on θ . We solve the optimization problem summarized in Algorithm 2, using the quasi-Newton method L-BFGS, as implemented in `scipy`, with gradients computed by automatic differentiation with `Pytorch` [Paszke et al. 2019]. We use `torchcubicspline` [Kidger 2017] for a differentiable cubic spline implementation.

For designs where symmetry should be explicitly preserved, we parametrize an n -fold symmetric configuration by a corresponding n -fold reduction of the number of optimization variables. The models shown in Figures 9, 12, 15, 19 make use of such changes of variables for symmetry enforcement.

For more information about the discretization choices used for each example, we refer to Table 1 on page 16. The full source code of

our implementation as well as example models shown in the paper are publicly available at <https://go.epfl.ch/c-tubes>.

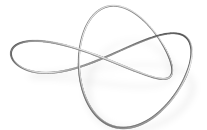
4.3 Optimization of M-Tubes

We illustrate the optimization process starting from the special case of M-tubes. Recall that M-tubes result from the natural choice of setting the apex locating function to $\mathbf{a} = 1$ and aligning the plane normals with the tangents of the directrix in the smooth case, or with the normals of the bisecting planes in the discrete case, see Section 2.3. As for any Monge surface, a directrix $\mathbf{X}(t)$ and a generatrix $\mathbf{G}_{:,0}$ are the only inputs necessary for the computation of an M-tube. In general, we assume these curves to be provided by the user. Note that a closed directrix does not guarantee closure of the corresponding Monge surface since in general the cross-sections do not match at the ends [Klok 1986].

To outline the structure of our design framework, we consider the problem of taking a closed input directrix and finding its best approximation according to a given metric that guarantees smooth closure of the corresponding M-tube.

4.3.1 Smoothly Closed Tubular Trefoil. Consider the parametrization of a trefoil knot

$$\widehat{\mathbf{X}}(t) = \begin{bmatrix} \cos t + 2 \cos 2t \\ \sin t - 2 \sin 2t \\ -\sin 3t \end{bmatrix} \text{ for } t \in [0, 2\pi].$$



An M-tube that has $\widehat{\mathbf{X}}(t)$ as its directrix would not close up smoothly. We measure the mismatch between the two ends of the tube as the defect angle φ corresponding to the angle between the initial and final directors of any rotation minimizing frame defined on the curve, see Figure 9, left. Note that φ is an intrinsic property of the directrix curve, which does not depend on the choice of the generatrix, nor on its initial rotation about the tangent¹. In particular, if $\mathbf{G}_{:,0}$ is the regular n -gon centered at $\mathbf{X}(t_0)$, the defect angle φ^* that

¹For smooth closed curves, φ can be computed as the integral of the curve torsion modulo 2π , see e.g. [Pinkall and Gross 2024].

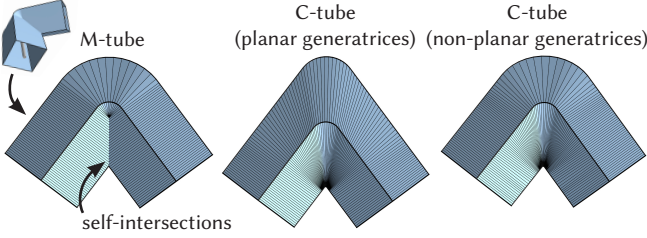


Fig. 10. When the directrix is highly curved, the M-tube construction can lead to self-intersections and fold-overs in some boundary strips (left). Starting from this degenerate configuration, our approach can recover structures free from local intersections satisfying the same boundary constraints. Limiting the choice to planar generatrices can produce deviations from the desired shape (center). By relaxing the planarity assumption, we can improve the approximation (right).

guarantees smooth closure of the M-tube must be a multiple of $2\pi/n$. In this section, we focus on the equilateral triangular generatrix and hence $n = 3$. A different choice of the cross-section would modify the set of admissible values for the defect angle φ^* . The conclusions we draw remain valid for any n , as well as for generatrices without radial symmetry, for which the defect angle must be an integer multiple of 2π for the C-tube to close up smoothly.

Specific classes of curves can be constructed to have a prescribed value of φ [Brander and Gravesen 2018]. However, finding a space curve having a specific value of φ that meanwhile approximates a target curve is in general a challenging task, which cannot be easily accomplished neither by manual exploration using standard CAD software, nor analytically. We propose to tackle this problem using numerical optimization.

4.3.2 Optimization of the Directrix Curve. To parametrize the set of directrix curves, we use a cubic spline with K points and sample it at M locations. We set K sufficiently high to capture the shape of the desired directrix curve, yet low enough to exclude unwanted high-frequency oscillations from the design space. The strips are in general discretized with high resolution to obtain a faithful approximation of their smooth counterparts, so $M > K$. Note that both K and M affect the number of optimization variables: While K determines the number of optimized points, M sets the number of plane normals and apex-locating function samples. Differently from the case of M-tubes, where the only free parameters are the K points, in C-tubes the number of optimization variables is then usually dominated by M .

We set the initial samples \mathbf{X} as target values for the directrix curve, assigning $\mathbf{X}_{\text{target}} \leftarrow \mathbf{X}$. Our aim is to optimize \mathbf{X} through the dependency on the points \mathbf{Q} , while limiting the deviation from $\mathbf{X}_{\text{target}}$, which we keep fixed.

Distance Constraints. We introduce two measures to capture desired geometric features. Recall that the *one-sided* squared chamfer distance between two sets of points \mathbf{X} and \mathbf{Y} of size M is defined as

$$d_C(\mathbf{X}, \mathbf{Y}) = \frac{1}{M} \sum_{i=0}^{M-1} \min_{j \in \{0, \dots, M-1\}} \|\mathbf{X}_i - \mathbf{Y}_j\|^2.$$

The *symmetric* squared chamfer distance can then be computed as $d(\mathbf{X}, \mathbf{Y}) = d_C(\mathbf{X}, \mathbf{Y}) + d_C(\mathbf{Y}, \mathbf{X})$.

The mismatch between the directrix and the target curve is then measured as

$$\mathcal{T}(\mathbf{X}) = \frac{1}{2B^2} d(\mathbf{X}, \mathbf{X}_{\text{target}}), \quad (5)$$

where the problem-dependent scaling constant B corresponds to the length of the bounding box diagonal of $\mathbf{X}_{\text{target}}$. Consequently, our fitting objective \mathcal{T} both keeps the directrix close to the target curve and ensures that it does not collapse onto a portion of the target curve.

Similarly, we measure the mismatch between the initial and final generatrices as

$$C(\mathbf{G}) = \frac{1}{2D^2} d(\mathbf{G}_{:,0}, \mathbf{G}_{:,M-1}), \quad (6)$$

where D is the bounding box diagonal of the 2D polyline $\mathbf{G}_{:,0}$, chosen to represent the thickness of the tube. Note that, if $\mathbf{G}_{:,0}$ and $\mathbf{G}_{:,M-1}$ are regular polygons, then $C(\mathbf{G})$ is left unchanged by cyclic permutations of the vertices: Defect angles φ that are multiples of $2\pi/n$ result in $C(\mathbf{G}) = 0$ if $\mathbf{G}_{:,0}$ is the regular n -gon.

Alternatively, the exact value of the defect angle can be enforced by measuring the Euclidean distance between pairs of vertices, for example as

$$\tilde{C}(\mathbf{G}) = \frac{1}{2ND^2} \sum_{i=0}^{N-1} \|\mathbf{G}_{i,0} - \mathbf{G}_{i,M-1}\|^2, \quad (7)$$

which enforces individual closure of all gluing curves.

Local Self-Intersections. If the curvature of the directrix is high, the boundary strips can self-intersect, as shown in Figure 10, left. In such cases the strips are not suitable for fabrication.

While in M-tubes the discrete gluing curves and the directrix are parallel by construction, they can have opposite orientations. To avoid encountering these configurations during the optimization, we introduce a penalty term that ensures that they point in the same direction. For practical and numerical reasons, we also enforce that the edges of the discrete gluing curves have a minimal length.

To this end, we consider the unit-length edge vectors $\mathbf{E}_{i,j} = (\mathbf{G}_{i,j+1} - \mathbf{G}_{i,j}) / \|\mathbf{G}_{i,j+1} - \mathbf{G}_{i,j}\|$ and the directrix tangent $\mathbf{T}_j = (\mathbf{X}_{j+1} - \mathbf{X}_j) / \|\mathbf{X}_{j+1} - \mathbf{X}_j\|$. We define the signed distance $l_{i,j} = \text{sign}(\mathbf{E}_{i,j} \cdot \mathbf{T}_j) \|\mathbf{G}_{i,j+1} - \mathbf{G}_{i,j}\|$ and penalize deviations using

$$\mathcal{R}(\mathbf{G}) = \frac{1}{2NM} \sum_{i=0}^{N-1} \sum_{j=0}^{M-1} \min(0, l_{i,j} - l_{\min})^2, \quad (8)$$

where l_{\min} is a small positive constant that defines the minimum length of the edge vectors.

This regularization term also applies to C-tubes, as discussed in the following section. It is included in all our examples but does not contribute to the objective function when all gluing curve edges exceed the minimum length and exhibit the desired alignment.

Problem Setup. The M-tube optimization problem is then formulated as

$$\min_{\mathbf{Q}} \tilde{\mathcal{J}}(\mathbf{Q}), \quad (9)$$

with

$$\tilde{J}(Q) = w_T \mathcal{T}(X(Q)) + w_C C(G(Q)) + w_R R(G(Q)),$$

where w_T , w_C , and w_R are weight parameters that control the relative importance of each objective.

In Figure 9, we show the result of the optimization and compare it with the initial M-tube. The optimized tube is smoothly closed. The value of the defect angle after optimization is $\varphi^* = 4\pi/3$, namely the multiple of $2\pi/3$ closest to the initial value of φ . As shown in the same figure, center, integer closure, i.e. $\varphi^* = 2\pi$, is achieved at the expense of a more pronounced deviation from X_{target} ; a consequence of $\tilde{C}(G) \geq C(G)$ for all G .

4.4 Optimization of General C-Tubes

M-tubes are only a subset of the possible geometries achieved with C-tubes. In general, the plane normals can be tilted with respect to the directrix tangent, and the apex-locating function can encode general cones, making the size and orientation of the sweep surface vary along the tube. Our construction parametrizes these additional degrees of freedom, which we can use to expand the design space of C-tubes.

This extra design freedom also introduces more possibilities for undesired configurations, potentially yielding C-tubes whose support or boundary strips exhibit singularities. We note that the regularization term (8) directly extends to the case of C-tubes. In this general case, however, in addition to ensuring the desired length of the gluing curve edges, it also beneficially aligns the tangents of the directrix with those of the gluing curves.

In the following, we continue the exposition of our optimization process, using the problem of generating a smoothly closed C-tube as an example, by relaxing the default choices for the plane normals and the apex-locating function. To better appreciate the effect of each type of degrees of freedom on the resulting design in isolation, we freeze the directrix points Q in their initial state. For the remaining of this section we then have $\mathcal{T}(X) = 0$.

4.4.1 Optimization of the Plane Normals. The plane normals P_j , previously coinciding with the tangent of the directrix (see Section 4.3.2), can be optimized to achieve a desired generatrix orientation along the sweep. For illustration purposes, we pick a single plane normal P_j at each directrix point X_j to keep the generatrices $\{G_{:,j}\}_{j=0}^{M-1}$ planar. Our observations straightforwardly generalize to the case of non-planar generatrices discussed, e.g., in Figure 10. For the moment, we also keep the apex-locating function constant and unitary. Our goal is to find P resulting in $C(G) = 0$.

Regularization. To regularize the problem further, we additionally ask that each plane normal P_j evolves smoothly along the directrix by penalizing variations as

$$\mathcal{L}(P) = \sum_{j=1}^{M-2} \|P_{j+1} + P_{j-1} - 2P_j\|^2. \quad (10)$$

Problem Setup. We optimize the plane normals for the tube to close up smoothly by solving the optimization problem

$$\min_P \tilde{J}(P), \quad (11)$$

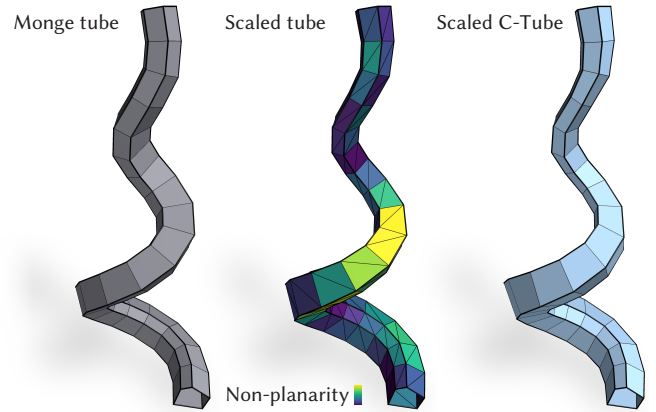


Fig. 11. Editing the developable M-tube on the left by scaling the profile polygons yields non-planar quads. Our optimization computes the values of the plane normals P and of the apex-locating function a that result in the desired cross-section scaling, while preserving exact developability of the strips and boundary conditions. The quad non-planarity is computed according to the measure introduced by Pottman and coauthors [2008].

with

$$\tilde{J}(P) = w_{\tilde{C}} \tilde{C}(G(P)) + w_R R(G(P)) + w_L \mathcal{L}(P).$$

Figure 9, center right, shows the result of the corresponding optimization, where the directrix X is held fixed in its initial configuration shown on the left of the same figure. Note how the choice of using \tilde{C} to enforce integer closure makes the strips connect back to themselves across the connection, forming three closed loops. However, differently from the Monge case with integer closure, the overall shape of the tube is now smoother. As a consequence of the deviation of P from the directrix tangent, the shape of the cross-section now varies along the sweep, generating a tube with variable thickness.

4.4.2 Optimization of the Apex-Locating Function. The thickness of the cross-section is in general out of the control of the designer when the only variables are the plane normals. We can use the values of the apex-locating function a as additional degrees of freedom to better control the cross-sectional profile of the tube.

Cross-Section Diameter Constraint. To measure the cross-section size, we first project each generatrix curve $G_{:,j}$ onto the bisecting plane between the two directrix edges $j-1$ and j to obtain $G_{:,j}^\perp$. This projection factors out length changes due to shearing, an effect that is more pronounced the more the plane normals deviate from the directrix tangent. We then define the cross-section diameter at t_j as the maximum distance between any two of the projected vertices

$$d_j = \max_{i_1, i_2} \|G_{i_1, j}^\perp - G_{i_2, j}^\perp\|.$$

We prescribe a uniform target cross-section diameter d_{target} , and penalize deviations quadratically as

$$\mathcal{D}(G) = \frac{1}{2} \sum_{j=0}^{M-1} (d_j - d_{target})^2. \quad (12)$$

Regularization. To ensure the tube radius varies smoothly, we additionally regularize the apex-locating function by penalizing its variations as

$$\mathcal{L}(\mathbf{a}) = \sum_{j=1}^{M-2} (a_{j+1} + a_{j-1} - 2a_j)^2. \quad (13)$$

Problem Setup. Closing a tube with prescribed diameter now consists of solving the optimization problem

$$\min_{\mathbf{P}, \mathbf{a}} \tilde{\mathcal{J}}(\mathbf{P}, \mathbf{a}), \quad (14)$$

where

$$\tilde{\mathcal{J}}(\mathbf{P}, \mathbf{a}) = w_{\mathcal{D}} \mathcal{D}(\mathbf{G}) + w_{\tilde{\mathcal{C}}} \tilde{\mathcal{C}}(\mathbf{G}) + w_{\mathcal{R}} \mathcal{R}(\mathbf{G}) + w_{\mathcal{L}} \mathcal{L}(\mathbf{a}),$$

where \mathbf{G} depends on \mathbf{P} and \mathbf{a} . Note that in general, rescaling each cross-section independently would break the PQ-ness of the strips and result in non-developable strips, as illustrated in Figure 11. In contrast, our construction guarantees that the strips composing the tube remain PQ.

For the example shown in Figure 9, we input the solution from Equation (11) into our algorithm and optimize for \mathbf{a} to obtain a more uniform cross-section size along the sweep, while preserving smooth closure at the connection.

We refer to Section 5 for more examples of C-tube design, including cases in which \mathbf{Q} , \mathbf{P} , and \mathbf{a} are optimized concurrently to satisfy multiple design objectives and constraints.

4.5 Alignment Constraints

To support effective design exploration and form-finding, we incorporate additional user control through targeted constraint functions for surface and tangency alignment.

Surface Alignment. Instead of measuring the spatial distance of the directrix to a given target curve as in Equation (5), it can be convenient to specify a reference surface S that the directrix can slide onto (see also Figure 17). Consider a boundary strip D_i and the two gluing curves associated to it, $G_{i,:}$ and $G_{i+1,:}$. The alignment of D_i to a surface S can be enforced by a penalty term that attracts $G_{i,:}$ and $G_{i+1,:}$ to S as

$$\mathcal{S}(\mathbf{G}) = \frac{1}{4M} \sum_{j=0}^{M-1} d_S(G_{i,j})^2 + d_S(G_{i+1,j})^2 \quad (15)$$

where $d_S : \mathbb{R}^3 \rightarrow \mathbb{R}$ is the point-to-surface distance. In combination with the exact planarity of the quads resulting from our construction, this formulation enforces tangency whenever the reference surface is itself developable. An example in which a boundary strip is fitted to a minimal surface is shown in Figure 17.

Orientation Alignment. The orientation in space of the developable strips is an important means to communicate design intent. Consider a boundary strip and the corresponding discretized PQ strip, and let \mathbf{n}_j be the normal of quad j . We enforce strip alignment by minimizing the angle between \mathbf{n}_j and a prescribed direction $\bar{\mathbf{n}}_j$. The alignment penalty takes the form

$$\mathcal{A}(\mathbf{G}) = \frac{1}{2|\mathcal{J}|} \sum_{j \in \mathcal{J}} (1 - \mathbf{n}_j \cdot \bar{\mathbf{n}}_j)^2, \quad (16)$$

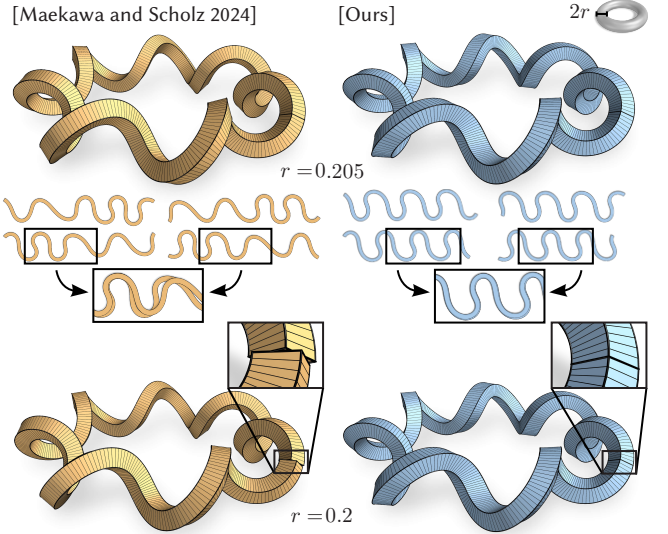


Fig. 12. Comparison of the method of [Maekawa and Scholz 2024] based on rotation-minimizing frames (left) with our approach (right). The directrix winds around a torus with major radius 1 and minor radius r . Since the rotation-minimizing frames only align for specific values (here $r = 0.205$), the resulting surface strips are in general discontinuous, as shown in the zoom. Our approach can optimize for closure for any value of r and additionally ensure that the strips are locally congruent, as illustrated in the overlays. The result on the top left has been recreated from Figures 23 and 24 of [Maekawa and Scholz 2024].

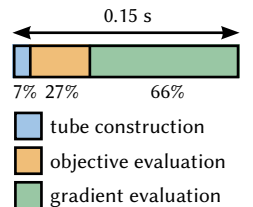
where $\mathcal{J} \subset \{0, \dots, M-2\}$ is a user-defined set of indices. The effect of this constraint is shown in Figure 15. The same constraint straightforwardly generalizes to the cases in which $\bar{\mathbf{n}}$ is the normal of another quad, effectively enforcing tangency between two boundary strips, as shown in Figure 16.

5 RESULTS

In this section we show results and highlight potential applications of our method. We specifically illustrate how designs can rely on the simplicity of fabrication of C-tubes and meanwhile meet advanced functional or aesthetic constraints.

The optimization takes seconds to few minutes to complete for all the examples shown in this section. A typical forward construction call is extremely fast to execute, and most of the computational time is spent in evaluating the objective function and its gradient, as can be seen in the inset figure, which represents the average iteration of the optimized design in Figure 15. Total runtimes on an Apple Macbook Pro with an 8-core M1 CPU are given in Table 1 on page 16. The same table collects the number of variables and the penalty and regularization terms used in each example.

The larger flexibility of C-tubes compared to M-tubes is exemplified in Figure 12, where we show a comparison with a result of the



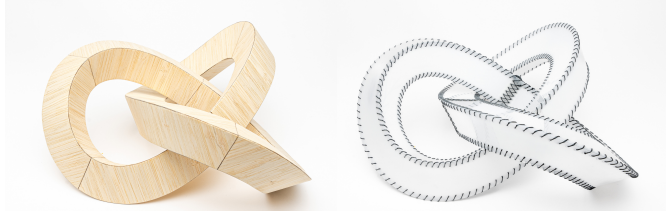


Fig. 13. Two physical models of a trefoil knot C-tube (approx. 20cm in diameter). The model on the left is constructed from cardboard-backed bamboo veneer, while the model on the right is made from POM-C, with the gluing curves stitched together using fishing line.

recent method of [Mackawa and Scholz 2024]. Since their construction employs rotation-minimizing frames, the resulting surfaces are restricted to Monge surfaces, offering no direct control to enforce a closure condition. Closed surfaces can thus only be obtained by carefully selecting the input directrix: The toroidal tube shown at the top left is created by searching for a suitable torus aspect ratio via bisection. In contrast, our method allows optimizing for continuous C-tubes using plane normals as extra degrees of freedom, for any closed input curve. The additional flexibility can yield other benefits. For example, even though the input curve is seven-fold symmetric, the unrolled Monge strips do not exhibit this symmetry. In our constructions, we constrain the tubular surface to turn by an exact multiple of $\pi/2$ in each of the seven lobes, yielding fully symmetric strips that can reduce fabrication complexity.

Optimizing for smooth closure is also a key aspect of the lamp design of Figure 1, which is a physical realization of the trefoil knot of Figure 9, second from the left. This model is composed of a single developable strip that we split into 7 segments, which are lasercut from translucent Polyoxymethylene (POM-C) sheet material. Interlocking zipper tab extensions are added to simplify assembly. Despite the very low bending stiffness of the material, the assembled structure is stiff and retains its shape, even under the additional load of the internal light tube which at 1.1kg is more than five times the weight of the C-tube.

Figure 13 shows two additional realizations of trefoil C-tubes, both based on the optimized directrix curve from Figure 9, second from the left. To simplify fabrication, the generatrix has been uniformly scaled by a factor of approximately two in both cases. The model on the left is constructed from cardboard-backed bamboo veneer, with the gluing curves joined edge to edge using wood glue. The model on the right is made from POM-C, using fishing line to connect the developable strips.

Scaling of the Generatrix. In Figure 14 we illustrate how a complex 3D surface can be realized as a C-tube by adaptive scaling of the generatrix (see also Figure 9, right). Specifically, we use the smooth reference surface to determine appropriate scaling factors for the hexagonal profile curve. The optimization then solves for the remaining parameters so that the resulting surface strips best approximate the design surface. The physical model is assembled from laser-cut paper strips.

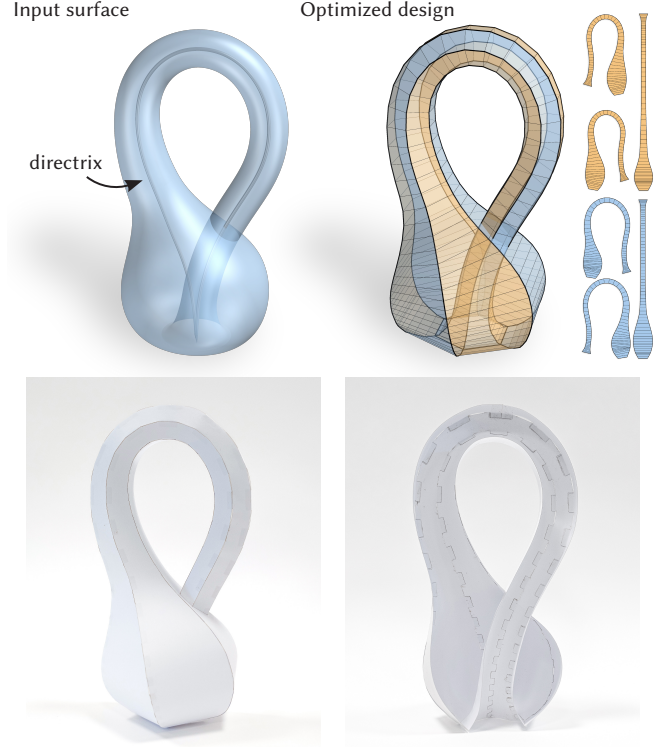


Fig. 14. Scaling the profile curve along the directrix allows approximating more complex tubular structures like this model of the Klein bottle. With a hexagonal generatrix we obtain the six developable strips depicted on the right. The physical model shown in the bottom row is made from paper.

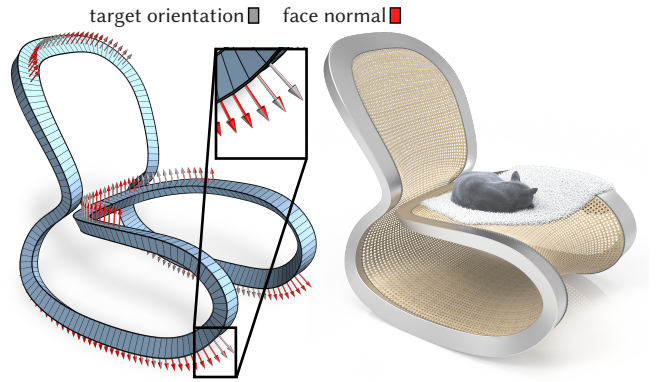


Fig. 15. A rocking chair composed of a C-Tube frame with an attached fabric. The alignment constraints used in the optimization are shown on the left.

Tangency Alignment. In Figure 15 we show an application in furniture design. We exploit the design freedom of C-tubes to enforce the alignment constraints from Eq. (16) that are essential for the function of the rocking chair. In particular, the optimization solves for the strip surface of the C-tube frame to be in continuous contact

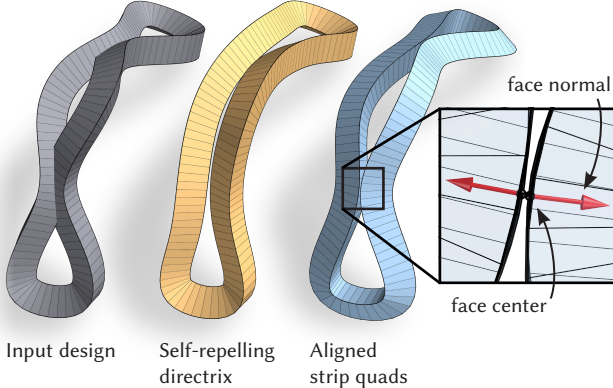


Fig. 16. Alignment optimization within a C-tube. Without additional constraints, the construction produces a self-intersecting surface (left). By adding self-repulsion to the directrix with minimal separation of two times the tube radius, the intersections can be removed, but the structure substantially deviates from the original design (center). By enforcing tangency alignment and minimal quad distance at two points along the curve, our optimization yields a valid result that better preserves the input shape (right).

with the ground during the desired rocking motion. Additional alignment constraints ensure that one of the strips faces in the direction of the user in the seat and headrest regions and that the fabric can be attached to the frame without creases.

Figure 16 illustrates the effect of intra-strip alignment. The direction of the quad normals is not prescribed, and two sections of a boundary strip can co-evolve to find their best orientation in space. Additionally, to guarantee physical separation, we enforce a minimal distance constraint between the two centroids of the quads involved in the alignment. The corresponding penalty term is computed as the squared difference between the desired separation \bar{d} and the signed centroid distance, where the sign is determined from the quad normals to prevent self-penetrated states. In this case we set $\bar{d} = 0.1r$, where r is the radius of the circle circumscribed to the equilateral triangle used as generatrix. We compare the result with the C-tube obtained using a self-repelling constraint on the directrix, with minimal separation of two times the tube radius, and show how the strip alignment better preserves the input shape.

In Figure 17, we deliberately aim to match the developable strips of a C-tube to a non-developable surface, a minimal surface of zero mean curvature, but non-zero Gaussian curvature. One of the boundary strips is aligned to the reference surface by the penalty term (15), while an adjacent gluing curve is attracted by the surface boundary. This example illustrates trade-offs in the optimization between tangential alignment to the reference surface and positional alignment to its boundary curve.

Framework for Casting. Instead of directly using C-tubes as structural elements, they can also function as molds for casting. In Figure 2 we show a design study of a lighting fixture, where scaling factors have been prescribed to avoid self-intersections in the tight regions of the knotted directrix. We envision C-tubes being used to create molds for casting concrete beams with freeform geometries,

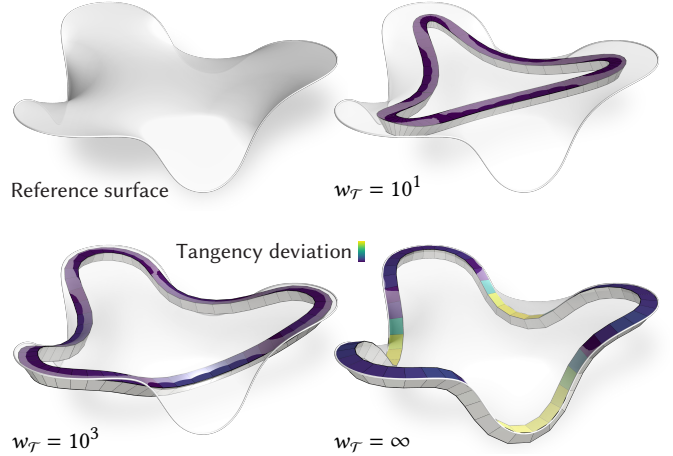


Fig. 17. Form-finding on a given reference surface. C-tubes are optimized to simultaneously keep one of the gluing curves close to the boundary of the reference surface (controlled by the weight w_T) and align one of the adjacent strips to the surface normal. Since no perfect alignment is possible to this non-developable surface, these conflicting objectives should be balanced by adjusting the alignment weights.

providing both structural and aesthetic benefits, while simplifying the construction process and reducing fabrication costs.

Support Structures. In Appendix C, we show how our construction implicitly defines a design space for developable and torsion-free support structures. Figure 18 illustrates how such supports can be integrated into a design, which is particularly relevant for large-scale constructions, e.g., in architecture.

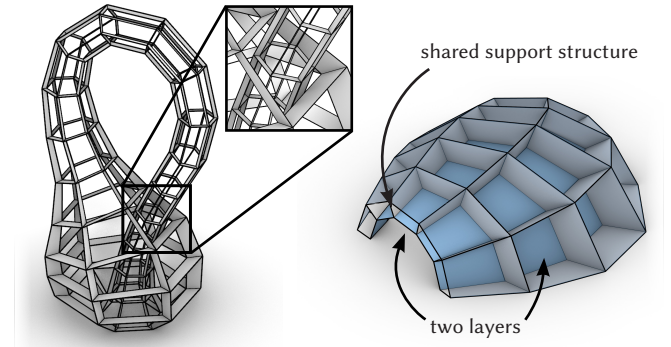


Fig. 18. Illustration of torsion-free support structures for a C-tube (left) and a cone net (right) generated by our construction. The figure on the right demonstrates how cone nets can support the formation of a second layer of planar faces, which also forms a cone net sharing the same support structure. Alternatively, this double-layer cone net can also be generated using the C-tube construction with non-manifold generatrices, as displayed in Figure 20.

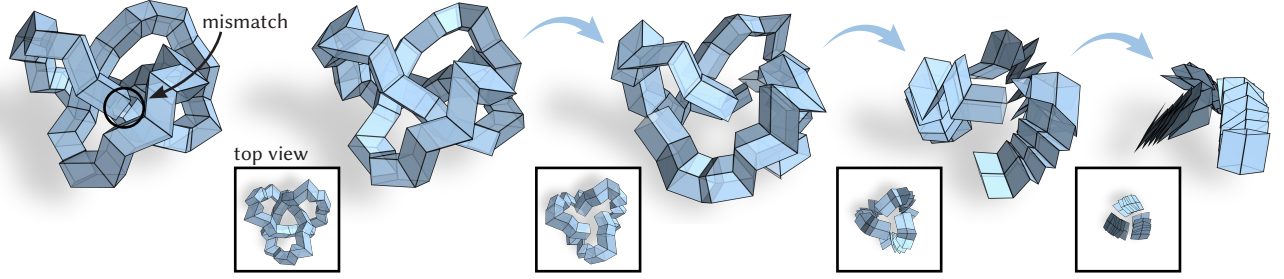


Fig. 19. Foldable zig-zagged C-tubes. Left: Discrete M-tube with a square generatrix along a zig-zagged polyline approximating a trefoil. Right: The rigid and flat-foldable M-tube optimized for closure and 3-fold rotational symmetry, along with its folding motion.

Deployable C-Tubes. C-tubes encompass a broad class of deployable surfaces that display rigid foldability. For instance, discrete M-tubes with rhomboidal cross-section are both rigid and flat-foldable, as discussed in [Filipov et al. 2015] and [Tachi 2011]. In the latter work, it is noted that more well-behaved folding motions can be obtained when selecting a zig-zag curve as the directrix.

Figure 19 (left) shows such a rigid-foldable M-tube. However, the constructed tube fails to align at the ends and does not preserve the three-fold symmetry of the directrix. Furthermore, it exhibits self-intersections during the folding motion. In Figure 19 (right), we show how our method can be used to optimize the directrix for closure and 3-fold rotational symmetry, while preserving flat-foldability. The exact symmetry allows splitting the tube into three congruent lobes, which can be folded independently without any self-intersections, and then assembled to form the final structure.

Non-manifold Generatrix. Figure 20 shows that the generatrix of a C-tube is not limited to simple polygons, offering additional flexibility for design exploration. Here we create a double-layer hollow beam with connecting supports, where all surface strips are still strictly developable.

C-Tube Networks. Optimizing for the alignment of the start and end profiles also enables to connect multiple tubes to pre-defined nodes. Figure 21 shows such a construction, where identical joints are used to connect the ends of C-tube beams. We treat the position of the joints Y as additional free variables to be optimized. We employ a two-stage approach to first fit M-tubes to the complex alignment constraints imposed by the connectors, before fine-tuning the directrix and plane normals to obtain the final C-tube network.

5.1 Limitations and Future Work

The exact developability of the boundary and support patches is a key feature of our method that enables fabrication from planar sheet materials. However, for some materials that are bendable but also support a limited amount of stretch, this constraint can be too restrictive to explore the full design space. For such materials, algorithms that only ensure developability approximately, e.g. using soft constraints, might be more suitable.

Despite having presented ways to control and recover from local (Figure 10) and global (Figures 16 and 19) self-penetrated states in the optimization process, we do not explicitly model non-physical intersections. Integrating methods for collision avoidance, such

as [Li et al. 2020], into the optimization is therefore an important future work.

Another practical concern is the potential waste when cutting the surface patches from planar sheet material. Currently, we split and arrange patches manually to fit into the working volume of our laser cutter. While these tasks could potentially be automated using existing techniques, it would be interesting to directly integrate material efficiency objectives into the optimization. This would allow trading possibly stronger deviations from the input design for more efficient material use.

One of the main benefits of tubular structures is their high stiffness to weight ratio. Our current approach is purely geometric and does not incorporate load-bearing capabilities of the resulting structures. An interesting avenue for future work would be to incorporate such aspects into our method to jointly optimize the shape and the mechanical performance of the resulting structures.

The simplicity of fabricating 3D structures from planar sheet material makes our technique not only relevant for industrial applications at large scales such as architectural constructions, but also empowers creative explorations for a general public. For example,

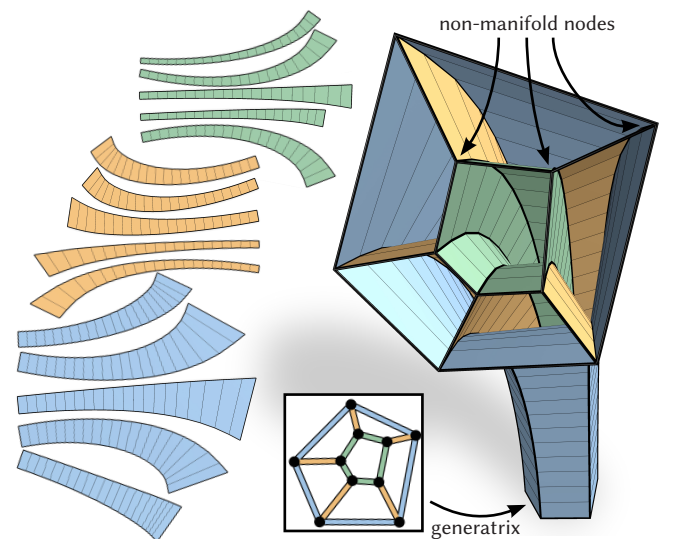


Fig. 20. Our method accommodates general line networks as generatrices.

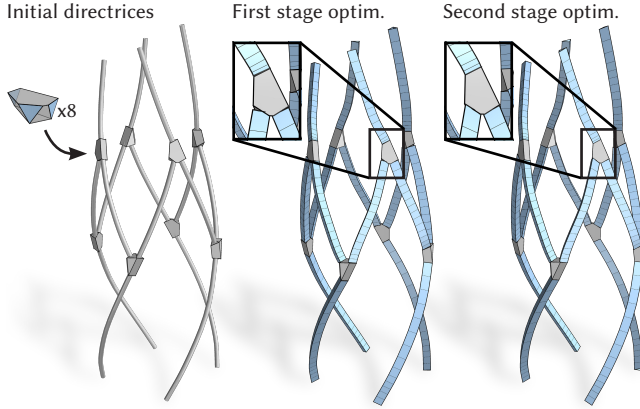


Fig. 21. A network of C-tubes. The shape of the connectors is fixed across the structure, but their position Y is free to be optimized to find the best alignment of the tubes. In a first stage, the optimization fits M-tubes to the connector geometry. The directrix and plane normals are then optimized to obtain the final C-tube network. The model is composed of 8 identical connectors and 16 C-tubes.

intricate C-tube designs can be fabricated simply by cutting and connecting strips of paper, which requires minimal equipment that is readily available even to hobbyists or children. Such widespread adoption requires further efforts to improve the performance of the implementation and in particular the design of a suitable visual interface that allows realtime design exploration with intuitive user feedback.

6 CONCLUSION

C-tubes are a versatile class of piecewise-developable surfaces with broad applicability and significant benefits for manufacturing and assembly. Our formulation introduces additional degrees of freedom to generalize existing constructions based on rotation-minimizing frames towards the broader class of cone-nets. This additional flexibility is essential to meet practical design objectives, such as avoiding discontinuities in closed C-tubes or enabling precise tangency or boundary alignments. Optimizing for such objectives is efficient, as we retain the simplicity of a constructive technique that is amenable to powerful numerical optimization techniques.

The consistent formulation of both discrete and continuous C-tubes establishes direct links to recent theoretical results and adds to the growing body of knowledge in discrete differential geometry. As such, C-tubes are a novel tool for both theoretical analysis and for practical applications in material- and fabrication-aware computational design.

ACKNOWLEDGMENTS

We gratefully acknowledge Erik Demaine and Tomohiro Tachi, whose idea of using scale mappings to encode the locations of cone apices forms the basis of our construction. We thank Liliane-Joy Dandy, Filip Goč, Oliver Gross, Uday Kusupati, Seiichi Suzuki, and Kurt Wettstein for their assistance with fabrication and valuable discussions.

This research was funded by the Swiss National Science Foundation (SNSF) grant numbers 200021-231293 and 200021_188582. Klara Mundilova is supported by the Swiss Government Excellence Scholarship.

REFERENCES

- E. Akleman, V. Srinivasan, J. Chen, and D. Victor. 2008. An Interactive Topological Mesh Modeler. In *Proceedings of Computer Graphics International (CGI '08)*.
- A. H. Bermano, T. Funkhouser, and S. Rusinkiewicz. 2017. State of the Art in Methods and Representations for Fabrication-Aware Design. *Computer Graphics Forum* 36, 2 (2017), 509–535.
- M. Bernhard and R. Maleczek. 2023. Multi-layered curved folding. *Proceedings of the IASS Annual Symposium 2023* 7 (2023), 1–11.
- A. I. Bobenko and Y. B. Suris. 2009. Discrete Koenigs nets and discrete isothermic surfaces. *International Mathematics Research Notices* 2009, 11 (2009), 1976–2012.
- D. Brander and J. Gravesen. 2017. Surfaces foliated by planar geodesics: a model for curved wood design. *Proceedings of Bridges 2017: Mathematics, Art, Music, Architecture, Education, Culture* (2017), 487–490.
- D. Brander and J. Gravesen. 2018. Monge surfaces and planar geodesic foliations. *Journal of Geometry* 109 (2018), 1–14.
- O. Böken. 1884. *Analytische Geometrie des Raumes*. A. Koch.
- S. Chandra, S. Bhooshan, and M. El-Sayed. 2015. Curve-folding polyhedra skeletons through smoothing. *Origami* 6 (2015), 231–240.
- E. D. Demaine, M. L. Demaine, D. A. Huffman, D. Koschitz, and T. Tachi. 2015. Characterization of curved creases and rulings: Design and analysis of lens tessellations. *Origami* 6 (2015), 209–230.
- E. D. Demaine, M. L. Demaine, D. A. Huffman, D. Koschitz, and T. Tachi. 2018. Conic crease patterns with reflecting rule lines. *Origami7: Proceedings of the 7th International Meeting on Origami in Science, Mathematics and Education (OSME 2018)* 2 (2018), 573–590.
- E. D. Demaine, M. L. Demaine, and D. Koschitz. 2011. Reconstructing David Huffman's legacy in curved-crease folding. *Origami* 5 (2011), 39–52.
- E. D. Demaine and G. N. Price. 2010. Generalized D-forms have no spurious creases. *Discrete & Computational Geometry* 43, 1 (2010), 179–186.
- E. T. Filipov, G. H. Paulino, and T. Tachi. 2016. Origami tubes with reconfigurable polygonal cross-sections. *Proceedings of the Royal Society A: Mathematical, Physical and Engineering Sciences* 472, 2185 (Jan. 2016), 20150607.
- E. T. Filipov, T. Tachi, and G. H. Paulino. 2015. Origami tubes assembled into stiff, yet reconfigurable structures and metamaterials. *Proceedings of the National Academy of Sciences* 112, 40 (Oct. 2015), 12321–12326.
- F. Gonzalez-Quintial and A. Martin-Pastor. 2024. Monge Surfaces. Generation, Discretisation and Application in Architecture. *Nexus Network Journal* 26 (2024), 811–828.
- H. Graf and R. Sauer. 1931. Über Flächenverbiegung in Analogie zur Verknickung offener Facettenfläche. *Mathematische Annalen*, 105 (1931), 499–535.
- H. Guggenheimer. 1989. Computing frames along a trajectory. *Computer Aided Geometric Design* 6, 1 (1989), 77–78.
- F. Huang, C. Jiang, T. Wills, and Y.-L. Yang. 2023. Forward and Inverse D-Form Modelling Based on Optimisation. *Computer-Aided Design* 157 (April 2023), 103467.
- A. Ion, M. Rabinovich, P. Herholz, and O. Sorkine-Hornung. 2020. Shape approximation by developable wrapping. *ACM Transactions on Graphics (TOG)* 39, 6 (2020).
- I. Izmostiev, A. Rasoulzadeh, and J. Tervooren. 2024. Isometric deformations of discrete and smooth T-surfaces. *Computational Geometry* 122 (2024), 102104.
- C. Jiang, K. Mundilova, F. Rist, J. Wallner, and H. Pottmann. 2019. Curve-pleated structures. *ACM Transactions on Graphics* 38, 6 (Dec. 2019), 1–13.
- C. Jiang, C. Wang, X. Tellier, J. Wallner, and H. Pottmann. 2022. Planar panels and planar supporting beams in architectural structures. *ACM Trans. Graph.* 1, 1 (Jan. 2022).
- P. Kidger. 2017. torchcubicspline. Last accessed 17 January 2025.
- M. Kilian, S. Flöry, Z. Chen, N. J. Mitra, A. Sheffer, and H. Pottmann. 2008. Curved folding. *ACM Transactions on Graphics* 27, 3 (Aug. 2008), 1–9.
- M. Kilian, C. Müller, and J. Tervooren. 2023. Smooth and Discrete Cone-Nets. *Results in Mathematics* 78 (2023).
- F. Klok. 1986. Two moving coordinate frames for sweeping along a 3D trajectory. *Computer Aided Geometric Design* 3 (1986), 217–229.
- D. Koschitz. 2014. *Computational design with curved creases : David Huffman's approach to paperfolding*. PhD thesis. MIT.
- M. Kraft, R. Maleczek, K. Mundilova, and T. Tachi. 2023. From Quad Filling to Wrinkled Surfaces. *Advances in Architectural Geometry* 6 (2023), 327.
- M. Li, Z. Ferguson, T. Schneider, T. Langlois, D. Zorin, D. Panozzo, C. Jiang, and D. M. Kaufman. 2020. Incremental potential contact: intersection-and inversion-free, large-deformation dynamics. *ACM Trans. Graph.* 39, 4, Article 49 (Aug. 2020), 20 pages.
- Y. Liu, H. Pottmann, J. Wallner, Y.-L. Yang, and W. Wang. 2006. Geometric modeling with conical meshes and developable surfaces. *ACM SIGGRAPH 2006 Papers* (2006), 681–689.

Table 1. Statistics of experiments shown in the paper: number of optimization iterations, number of spline points, number of directrix vertices, total optimization time, design variables, and terms included in the objective function. All the experiments include the term (8). Whenever P and a are optimized, the corresponding regularization terms (10) and (13) are also included. The symbol \star indicates the use of specific penalties described in the text. To define convergence, we set a gradient norm tolerance of 10^{-5} and a relative function reduction of 10^{-10} . An asterisk $*$ indicates that the maximum number of iterations was reached.

Figure	#iterations	#points (K)	#vertices (M)	optim. time (min:sec)	optim. variables	objective terms
2	2000*	30	146	01:28	Q, P, a	5, 6, 12
9 (center left)	9	3×6	3×66	00:01	Q	5, 6
9 (center)	47	3×6	3×66	00:05	Q	5, 7
9 (center right)	203	3×6	3×66	00:14	P	7
9 (right)	1000*	3×6	3×66	01:18	P, a	7, 12
10 (center)	1459	100	100	00:37	P	7
10 (right)	1254	100	100	00:29	P	7
11	416	11	22	00:17	P, a	7, 12
12 (top)	641	7×12	7×67	01:44	P	7
12 (bottom)	764	7×12	7×67	02:04	P	7
14	829	64	64	00:18	P, a	7, 12
15	1000*	2×17	2×129	02:39	P, a, θ	6, 12, 16
16 (center)	82	17	129	00:10	Q, θ	5, 7, \star
16 (right)	158	17	129	00:23	Q, θ	5, 7, 16, \star
17 (top right)	200*	65	65	00:12	Q, θ	5, 7, 15
17 (bottom left)	245	65	65	00:14	Q, θ	5, 7, 15
17 (bottom right)	5	65	65	00:01	θ	7, 15
19	69	13	13	00:23	Q	5, 7
21 (center)	1000*	16×6	16×15	01:36	Q, θ, Y	5, 6
21 (right)	5000*	16×6	16×15	05:25	Q, P, θ, Y	5, 6

- T. Maekawa and F. Scholz. 2024. All you need is rotation: Construction of developable strips. *ACM Transactions on Graphics* 43, 6 (2024).
- R. Mesnil, C. Douthe, O. Bavarot, and J.-F. Caron. 2015. Isogonal moulding surfaces: a family of shapes for high node congruence in free-form structures. *Automation in Construction* (2015).
- K. Mundilova. 2024. *Gluing and Creasing Paper along Curves: Computational Methods for Analysis and Design*. PhD thesis. MIT.
- A. Paszke, S. Gross, F. Massa, A. Lerer, J. Bradbury, G. Chanan, T. Killeen, Z. Lin, N. Gimelshein, L. Antiga, A. Desmaison, A. Kopf, E. Yang, Z. DeVito, M. Raison, A. Tejani, S. Chilamkurthy, B. Steiner, L. Fang, J. Bai, and S. Chintala. 2019. *PyTorch: an imperative style, high-performance deep learning library*. Curran Associates Inc., Red Hook, NY, USA.
- U. Pinkall and O. Gross. 2024. *Differential Geometry: From Elastic Curves to Willmore Surfaces*. Springer International Publishing, Cham.
- H. Pottmann. 2007. *Architectural Geometry*. Bentley Institute Press.
- H. Pottmann, A. Schiftner, P. Bo, H. Schmiedhofer, W. Wang, N. Baldassini, and J. Wallner. 2008. Freeform surfaces from single curved panels. *ACM Transactions on Graphics (TOG)* 27, 3 (2008), 1–10.
- H. Pottmann and J. Wallner. 2010. *Computational Line Geometry. Mathematics + Visualization* (2. auflage ed.). Springer.
- M. Rabinovich, T. Hoffmann, and O. Sorkine-Hornung. 2019. Modeling curved folding with freeform deformations. *ACM Transactions on Graphics (TOG)* 38, 6 (2019), 1–12.
- M. Raffaeli, J. Bohr, and S. Markvorsen. 2016. Sculpturing Surfaces with Cartan Ribbons. *Proceedings of Bridges 2016: Mathematics, Music, Art, Architecture, Education, Culture* (2016), 457–460.
- M. Raffaeli, J. Bohr, and S. Markvorsen. 2018. Cartan ribbonization and a topological inspection. *Proceedings of the Royal Society A* 474, 2220 (2018).
- K. Rose, A. Sheffer, J. Wither, M.-P. Cani, and B. Thibert. 2007. Developable surfaces from arbitrary sketched boundaries. *SGP'07-5th Eurographics Symposium on Geometry Processing* (2007), 163 – 172.
- R. Sauer. 1942. Streifenmodelle und Stangenmodelle zur Differentialgeometrie der Drehflächen, Schraubenflächen und Regelflächen. *Mathematische Zeitschrift* 48, 1 (1942), 455–466.
- S. Sellán, N. Aigerman, and A. Jacobson. 2020. Developability of heightfields via rank minimization. *ACM Trans. Graph.* 39, 4 (2020), 109.
- K. Sharifmoghadam, R. Maleczek, and G. Nawratil. 2023. Generalizing rigid-foldable tubular structures of T-hedral type. *Mechanics Research Communications* 132 (2023), 104151.
- K. Sharifmoghadam, G. Nawratil, A. Rasoulzadeh, and J. Tervooren. 2020. Using flexible trapezoidal quad-surfaces for transformable design. *Proceedings of IASS annual symposia* 2020, 28 (2020), 1–13.
- J. Solomon, E. Vouga, M. Wardetzky, and E. Grinspun. 2012. Flexible developable surfaces. *Computer Graphics Forum* 31, 5 (2012), 1567–1576.
- O. Stein, E. Grinspun, and K. Crane. 2018. Developability of triangle meshes. *ACM Transactions on Graphics* 37, 4 (Aug. 2018), 1–14.
- G. Stern and R. Maleczek. 2018. Lens tessellation inspired surface approximation. *Origami7* 1 (2018), 865–876.
- T. Tachi. 2011. *One-DOF Rigid Foldable Structures from Space Curves*. Technical Report.
- T. Tachi. 2013. Composito Rigid-Foldable Curved Origami Structure. *Proceedings of Transformables* (2013), 18–20.
- T. Tachi. 2016. Designing Rigidly Foldable Horns Using Bricard's Octahedron. *J. Mechanisms Robotics* 8, 3 (June 2016), 6.
- C. Tang, P. Bo, J. Wallner, and H. Pottmann. 2016. Interactive design of developable surfaces. *ACM Transactions on Graphics (TOG)* 35, 2 (2016), 1–12.
- F. Verhoeven, A. Vaxman, T. Hoffmann, and O. Sorkine-Hornung. 2022. Dev2PQ: Planar quadrilateral strip remeshing of developable surfaces. *ACM Transactions on Graphics (TOG)* 41, 3 (2022), 1–18.
- T. Wills. 2006. D-Forms: 3D forms from two 2D sheets. *Bridges London: mathematics, music, art, architecture, culture* (2006), 503–510.
- Q. Xing, G. Esquivel, and E. Akleman. 2012. Twisted D-Forms: Design and Construction of D-Forms with Twisted Prismatic Handles with Developable Sides. In *Proceedings of Bridges 2012: Mathematics, Music, Art, Architecture, Culture*, 323–328.
- C. Yuan, N. Cao, and Y. Shi. 2023. A Survey of Developable Surfaces: From Shape Modeling to Manufacturing. arXiv:2304.09587

A DISCUSSION OF THE SCALE MAPPING APPROACH

As visualized in Section 2.2, cone-nets consist of parameter lines tangent to both cylinders and cones, with the parameter lines tangent to cylinders serving as a key design feature in freeform shapes. However, when examining the trajectories of cone apices, these trajectories become discontinuous at the cylindrical parameter lines, where they effectively “escape to infinity”, a property that has the potential to present computational challenges.

Our construction circumvents the explicit use of the cone apex trajectory by encoding the cone apices as points on the tangents of a more well-behaved curve, the directrix. This approach builds on the idea presented in [Mundilova 2024, Section 12.4], which analytically encodes the location of cone apices using scale transformations uniquely defined by two distinct points and a scalar value. Figure 22 illustrates the cone apex trajectory and the corresponding apex-locating function.

While this representation offers significant numerical advantages, it has a drawback, as noted in Section 3.3: on every tangent, there is one point that cannot be represented with a finite value of $a(t)$. Specifically, this point corresponds to the first point, A, in the definition of the scale mapping.

In the discussed construction, the points A are set to coincide with the directrix. As a result, points in the neighborhood around A correspond to high values of $a(t)$. Practically, this is advantageous, as experimental observations indicate that apices close to the directrix are undesirable, often leading to C-tubes that deviate significantly from the intended structure.

B DETAILS OF COMPUTATIONS IN SECTION 3.3.2

In this section, we discuss the computation of smooth C-tubes in greater detail, and show how to derive two differential equations and an algebraic condition, requiring two initial values for their computation. These initial values can be interpreted as the starting point of the gluing curve.

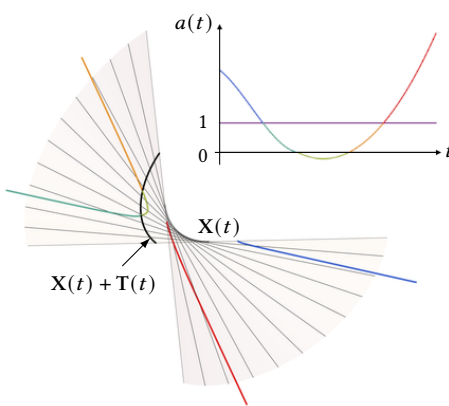


Fig. 22. Illustration of the apex locating function used to generate the smooth C-tube in Figure 4 and the corresponding trajectory of cone apices on the tangent developable of $X(t)$.

B.1 Outline

In the following, we assume that the gluing curves can be parametrized as curves on the developable support patches by

$$G_i(t) = X(t) + l_i(t)R_i(t),$$

with $G_i(t_0) := G_{i,0}$, where $l_i(t) : T \rightarrow \mathbb{R}$ and $R_i(t) : T \rightarrow S^2$ are an initially unknown length function and the initially unknown support patches' ruling directions, respectively.

The outline of our computation is as follows:

- *Step 1:* First, for a given directrix, we compute the rulings of the support patches. We will see that these ruling directions are determined by the developability requirement of the support patch.
- *Step 2:* Next, we compute the lengths $l_i(t)$ that ensure that the cone-apices lie on the corresponding tangents of the gluing curves, encoded by the apex locating function.

B.2 Step 1: Computation of the Ruling Directions

In the following, we assume without loss of generality that the directrix $X(t)$ is arc-length parametrized and that the unit normal vectors $P_i(t)$ of the planes are described in terms of two angular functions $\phi_i(t) \in C^1$ and $\psi_i(t) \in C^1$ with respect to the curves Frenet frame $(T(t), N(t), B(t))$ as

$$P_i(t) = \cos \phi_i(t) \cos \psi_i(t) T(t) + \cos \phi_i(t) \sin \psi_i(t) N(t) + \sin \phi_i(t) B(t).$$

Since $P_i(t) \cdot T(t) \neq 0$, it follows that $\psi_i(t), \phi_i(t) \neq \frac{\pi}{2} \pmod{\pi}$.

We encode the ruling directions $R_i(t) \in \Pi_i(t)$ using an initially unknown angular function $\xi_i(t)$ as

$$R_i(t) = \cos \xi_i(t) V_i(t) + \sin \xi_i(t) V_i^\perp(t),$$

where $V_i(t)$ and $V_i^\perp(t)$ are two orthogonal unit-length vectors that span the planes $\Pi_i(t)$. They are defined as

$$\begin{aligned} V_i(t) &= \frac{B(t) \times P_i(t)}{|B(t) \times P_i(t)|} \\ &= -\sin \psi_i(t) T(t) + \cos \psi_i(t) N(t) \end{aligned}$$

and

$$V_i^\perp(t) = P_i(t) \times V_i(t).$$

Note that $|B(t) \times P_i(t)| \neq 0$ since $T(t) \cdot P_i(t) \neq 0$.

The developability of the support patch can be expressed as

$$\det(T(t), R_i(t), R'_i(t)) = 0, \quad (17)$$

which translates to the following first-order differential equation for $\xi_i(t)$:

$$\xi'_i(t) = C_\tau(t) \tau(t) + C_k(t) k(t) + C_{\phi'}(t) \phi'_i(t) + C_{\psi'}(t) \psi'_i(t), \quad (18)$$

where

$$\begin{aligned} C_\tau &= -\frac{1}{2} (1 + \cos(2\psi_i) \cos(2\xi_i)) \sec \phi_i \sec \psi_i \\ &\quad - \cos \phi_i \cos \psi_i \sin^2 \xi_i + \tan \phi_i \sin \psi_i \sin(2\xi_i), \\ C_k &= -(\sin \phi_i \sin \xi_i + \tan \psi_i \cos \xi_i) \sin \xi_i, \\ C_{\phi'} &= (\tan \phi_i \cos \xi_i - \sec \phi_i \tan \psi_i \sin \xi_i) \sin \xi_i, \\ C_{\psi'} &= -(\sin \phi_i \sin \xi_i + \tan \psi_i \cos \xi_i) \sin \xi_i. \end{aligned}$$

Note that for well-behaved planes and appropriate curvature and torsion, we can locally find a solution for this angular function, and hence the ruling directions of the support patch.

When $\Pi_i(t)$ is the family of normal planes, $\psi_i(t) = \phi_i(t) = 0$, so that $\mathbf{V}_i(t) = \mathbf{N}(t)$ and $\mathbf{V}_i^\perp(t) = \mathbf{B}(t)$. In this case, Equation (18) simplifies to

$$\xi'_i(t) = -\tau(t),$$

corresponding to the result presented in [Guggenheim 1989], which details the computation of Klok's frame, now known as the rotation-minimizing frame of a space curve.

To match provided boundary conditions, we use the initial values

$$\xi(t_0) = \arctan(\mathbf{G}_i(t_0) \cdot \mathbf{V}_i(t_0), \mathbf{G}_i(t_0) \cdot \mathbf{V}_i^\perp(t_0)).$$

B.3 Step 2: Computation of the Length Function

In the following, our goal is to compute the length function $l_i(t)$, such that the vectors $\mathbf{G}'_i(t)$ and $\sigma_t(\mathbf{G}_i(t)) - \mathbf{G}_i(t)$ align (up to orientation). This condition is satisfied when their cross product is the null vector. Accordingly, we define:

$$\mathbf{E}_i(t) = \mathbf{G}'_i(t) \times (\sigma_t(\mathbf{G}_i(t)) - \mathbf{G}_i(t)).$$

Note that both vectors $\mathbf{G}'_i(t)$ and $\sigma_t(\mathbf{G}_i(t)) - \mathbf{G}_i(t)$ lie in the tangent plane of the corresponding developable support patch. Consequently, vector $\mathbf{E}_i(t)$ is perpendicular to the incident tangent plane. Aligning $\mathbf{G}'_i(t)$ and $\sigma_t(\mathbf{G}_i(t)) - \mathbf{G}_i(t)$ then amounts to setting the remaining non-tangential component of $\mathbf{E}_i(t)$ to zero. In the computations that follow, we express this condition and assume that the support patch does not have a singularity at $\mathbf{X}(t)$, that is, we assume that $\mathbf{T}(t)$ and $\mathbf{R}(t)$ are not aligned.

First, we simplify

$$\begin{aligned} \sigma_t(\mathbf{G}_i(t)) - \mathbf{G}_i(t) &= a(t)(\mathbf{G}_i(t) - \mathbf{X}(t) - \mathbf{T}(t)) + \mathbf{X}(t) - \mathbf{G}_i(t) \\ &= -(1-a(t))l_i(t)\mathbf{R}_i(t) + \mathbf{T}(t), \end{aligned}$$

which yields

$$\begin{aligned} \mathbf{E}_i &= (\mathbf{T} + l'_i\mathbf{R}_i + l_i\mathbf{R}'_i) \times (-(1-a)l_i\mathbf{R}_i + \mathbf{T}) \\ &= -((1-a)l_i + l'_i)(\mathbf{T} \times \mathbf{R}_i) - l_i(\mathbf{T} \times \mathbf{R}'_i) + (1-a)l_i^2(\mathbf{R}_i \times \mathbf{R}'_i). \end{aligned} \quad (19)$$

It follows from the developability condition in Equation (17) that the three vectors $\mathbf{T}(t) \times \mathbf{R}_i(t)$, $\mathbf{T}(t) \times \mathbf{R}'_i(t)$, and $\mathbf{R}_i(t) \times \mathbf{R}'_i(t)$ are orthogonal to the tangent plane of the support patch. We therefore consider the orthonormal frame $(\mathbf{T}(t), \mathbf{T}_i^\perp(t), \mathbf{T}(t) \times \mathbf{T}_i^\perp(t))$ of $\mathbf{X}(t)$ that is aligned with the tangent plane of the corresponding support patch, with

$$\mathbf{T}_i^\perp(t) = \frac{(\mathbf{T}(t) \times \mathbf{R}_i(t)) \times \mathbf{T}(t)}{|(\mathbf{T}(t) \times \mathbf{R}_i(t)) \times \mathbf{T}(t)|},$$

where

$$(\mathbf{T} \times \mathbf{R}_i) \times \mathbf{T} = (\cos \psi_i \cos \xi_i - \sin \phi_i \sin \psi_i \sin \xi_i) \mathbf{N} + \cos \phi_i \sin \xi_i \mathbf{B}.$$

Using the representation of a vector \mathbf{V} within the orthonormal frame $(\mathbf{T}, \mathbf{T}_i^\perp, \mathbf{T} \times \mathbf{T}_i^\perp)$ as

$$\mathbf{V} = (\mathbf{V} \cdot \mathbf{T})\mathbf{T} + (\mathbf{V} \cdot \mathbf{T}_i^\perp)\mathbf{T}_i^\perp + (\mathbf{V} \cdot (\mathbf{T} \times \mathbf{T}_i^\perp))(\mathbf{T} \times \mathbf{T}_i^\perp), \quad (20)$$

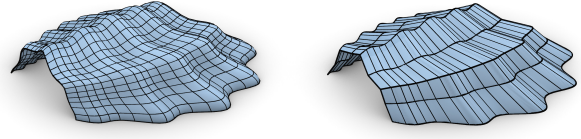


Fig. 23. A smooth and a semi-discrete cone-net computed in Mathematica.

we find

$$\begin{aligned} \mathbf{T} \times \mathbf{R}_i &= (\mathbf{T}^\perp \cdot \mathbf{R}_i)(\mathbf{T} \times \mathbf{T}_i^\perp), \\ \mathbf{T} \times \mathbf{R}'_i &= (\mathbf{T}^\perp \cdot \mathbf{R}'_i)(\mathbf{T} \times \mathbf{T}_i^\perp), \\ \mathbf{R}_i \times \mathbf{R}'_i &= ((\mathbf{T} \cdot \mathbf{R}_i)(\mathbf{T}_i^\perp \cdot \mathbf{R}'_i) - (\mathbf{T} \cdot \mathbf{R}'_i)(\mathbf{T}_i^\perp \cdot \mathbf{R}_i))(\mathbf{T} \times \mathbf{T}_i^\perp). \end{aligned}$$

The constraint that the non-tangential component of \mathbf{E}_i is zero can be expressed as $\mathbf{E}_i \cdot (\mathbf{T} \times \mathbf{T}_i^\perp) = 0$. Using Equation (19) this becomes

$$\begin{aligned} l'_i(\mathbf{T}_i^\perp \cdot \mathbf{R}_i) &= -(1-a)l_i(1 + l_i(\mathbf{T} \cdot \mathbf{R}'_i))(\mathbf{T}_i^\perp \cdot \mathbf{R}_i) \\ &\quad - l_i(1 - (1-a)l_i(\mathbf{T} \cdot \mathbf{R}_i))(\mathbf{T}_i^\perp \cdot \mathbf{R}'_i), \end{aligned} \quad (21)$$

where $\mathbf{T}_i^\perp \cdot \mathbf{R}_i \neq 0$, based on the assumption that no tangent of the directrix aligns with the ruling direction.

Consequently, it follows that

$$l'_i = -(1-a)l_i(1 + l_i(\mathbf{T} \cdot \mathbf{R}'_i)) - l_i(1 - (1-a)l_i(\mathbf{T} \cdot \mathbf{R}_i)) \frac{\mathbf{T}^\perp \cdot \mathbf{R}'_i}{\mathbf{T}^\perp \cdot \mathbf{R}}.$$

For sufficiently well-behaved right-hand sides, a unique local solution can be obtained.

Note that in the special case where $a(t) = 1$, that is, the smooth Monge tube case, this equation simplifies to

$$\frac{l'_i}{l_i} = -\frac{\mathbf{T}_i^\perp \cdot \mathbf{R}'_i}{\mathbf{T}_i^\perp \cdot \mathbf{R}_i}.$$

This differential equation describes a curve that is parallel to the directrix. In an equivalent form, it can be found for example in Lemma 2.5 in [Mundilova 2024]. Figure 23 shows illustrations of cone-nets computed analytically using differential equations in Mathematica.

C TORSION-FREE SUPPORT STRUCTURES OF C-TUBES

Large-scale physical realizations of PQ meshes, for example in architecture, typically require additional *support structures*. These can be realized as a collection of prismatic beams that follow the edges of the mesh and meet at nodes corresponding to the mesh vertices. Meshes with *torsion-free* support structures are particularly beneficial for their ease of fabrication and low stresses. In these meshes, the node axes of neighboring vertices are required to be coplanar, see [Pottmann 2007] and [Jiang et al. 2022].

Torsion-Free Support Structures for C-Tubes. A feature of our proposed C-tube construction is the straightforward extraction of node axes for torsion-free support structures. In the case of discrete C-tubes, selecting the incident rulings of the support patches as node axes results in torsion-free nodes. This directly follows from the construction, as adjacent node axes along the t -parameter directions are coplanar (see also Figure 4). Adjacent node axes along the u -parameter directions are also coplanar, as they converge at the corresponding point of the directrix.

In the case of smooth C-tubes, the smooth support patches correspond to a semi-discrete counterpart of torsion-free nodes, as the infinitesimally close node axes are coplanar.

Families of Torsion-Free Support Structures. Note that upon successful construction, the input described in Section 3.2 results in a single C-tube. However, this same C-tube can be generated from different combinations of inputs. For example, we obtain the same discrete C-tube if we individually change the construction planes, as long as they contain the rulings of the support patches. This allows for a single degree of freedom for each plane. In the smooth case, any changes must occur “smoothly” to maintain the stated differentiability requirements. Since these modifications do not affect the incident support patches, they also do not impact the support structures.

However, we can also obtain the same discrete C-tube with a different support structure by carefully modifying the directrix $X(t)$ to $\tilde{X}(t)$, the apex-locating function $a(t)$ to $\tilde{a}(t)$, and the families of planes $\Pi_i(t)$ to $\tilde{\Pi}_i(t)$, while preserving the cone-apex locations $C(t)$ (see Figure 24). For instance, we may choose $\tilde{X}(t_0)$ and adjust subsequent points $\tilde{X}(t_{j+1})$ while ensuring that the points $\tilde{X}(t_{j+1})$, $\tilde{X}(t_j)$, and $C(t_j)$ are collinear. This process is equivalent to finding the rulings of a PQ strip that pass through the target cone apices, and setting $\tilde{X}(t)$ to be its edge of regression.

Upon successful computation of a new directrix $\tilde{X}(t)$, the apex locating function $\tilde{a}(t)$ must be adjusted appropriately to ensure that the cone apices of the modified input are unchanged. Finally, the families of construction planes also require appropriate modification. Specifically, as discussed above, we obtain the given C-tube as long as the construction planes $\tilde{\Pi}_i(t_j)$ contain the line connecting $\tilde{X}(t_j)$ with the target gluing curve vertex $G_i(t_j)$.

D DOUBLE CONE-NETS AND C-TUBES

The construction presented in Section 3.3 produces smooth and discrete C-tubes, where the tangent planes along u -parameter lines, or PQ strips in the u -direction, respectively, lie within a discrete cone, forming semi-discrete and discrete tubular cone-nets. As mentioned before, in this context, closure is motivated by the application; the generatrix could also be an open curve.

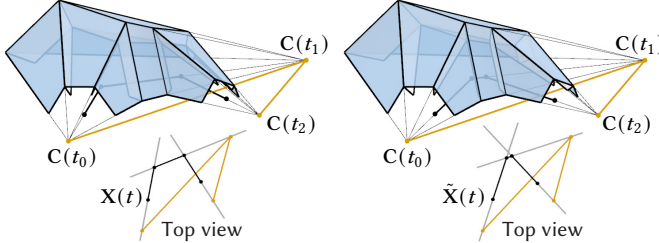


Fig. 24. Illustration of two identical discrete cone nets constructed using the C-tube method, each generated from a different directrix, resulting in distinct support structures. The directrices are related as distinct edges of regression of two discrete developable surfaces that pass through the set of common apices, connected by the yellow curve in the figure.

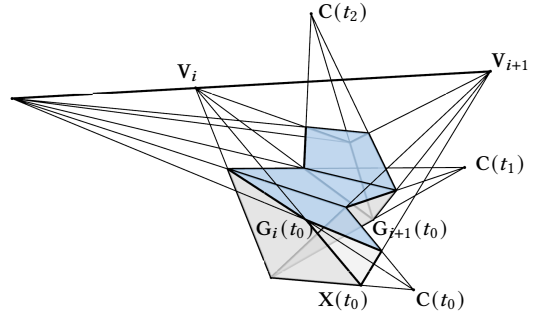


Fig. 25. The construction of a double cone-net using conical support patches.

We show how our construction can be used to generate a special subclass of cone-nets, the so-called double cone-nets, which are PQ meshes in which both families of PQ strips are contained in discrete cones. In Theorem 42 in [Kilian et al. 2023], the authors show that every double cone-net is a Koenigs net [Bobenko and Suris 2009].

We can obtain double cone-nets by a modification of the support patch construction. Specifically, we construct supporting patches that are either cylinders or cones with cone apices V_i . This can be achieved by either directly selecting the (real or infinite) cone apices or setting $\Pi_i(t_j)$ to represent an appropriate bundle of planes. Otherwise, the construction remains unchanged.

As a result, the boundary patches of the C-tube will also be conical. This is a direct consequence of the rulings of the boundary patches lying within the pencil of planes spanned by the (real or infinite) apices of the adjacent conical patches. In particular, the apex of the boundary strip is located at the intersection of the plane bundle’s axis and the first ruling direction (see Figure 25).